The climatology of small-scale orographic precipitation over the Olympic Mountains: Patterns and processes

Justin R. Minder,[a]* Dale R. Durran,[a] Gerard H. Roe[b] and Alison M. Anders[c]

[a] *Department of Atmospheric Science, University of Washington, USA*
[b] *Department of Earth and Space Science, University of Washington, USA*
[c] *Department of Geology, University of Illinois at Urbana Champaign, USA*

ABSTRACT: The climatology of small-scale patterns of mountain precipitation is poorly constrained, yet important for applications ranging from natural hazard assessment to understanding the geologic evolution of mountain ranges. Synthesizing four rainy seasons of high-resolution precipitation observations and mesoscale model output (from the Penn State/NCAR MM5), reveals a persistent small-scale pattern of precipitation over the ~10 km wide, ~800 m high ridges and valleys of the western Olympic Mountains, Washington State, USA. This pattern is characterized by a 50–70% excess accumulation over the ridge crests relative to the adjacent valleys in the annual mean. While the model shows excellent skill in simulating these patterns at seasonal time-scales, major errors exist for individual storms.

Investigation of a range of storm events has revealed the following mechanism for the climatological pattern. Regions of enhanced condensation of cloud water are produced by ascent in stable flow over the windward slopes of major ridges. Synoptically generated precipitation grows by collection within these clouds, leading to enhanced precipitation which is advected by the prevailing winds.

Instances of atypical patterns of precipitation suggest that under certain conditions (during periods with a low freezing level, or convective cells) fundamental changes in small-scale patterns may occur. However, case-studies and composite analysis suggest that departures from the pattern of ridge-top enhancement are rare; the basic patterns and processes appear robust to changes in temperature, winds, and background rainfall rates. Copyright © 2008 Royal Meteorological Society

KEY WORDS   MM5; mountain waves

Received 30 August 2007; Revised 1 February 2008; Accepted 11 April 2008

1. Introduction and background

The effect of small-scale topographic features on the distribution of precipitation was first recognized in the 1960s due to observations by Tor Bergeron's 'project Pluvius' rain-gauge network showing a 50% enhancement of precipitation over ~50 m high, ~10 km wide hills in Uppsala, Sweden (Bergeron, 1968). Advancement in understanding orographic precipitation on scales smaller than entire mountain ranges (scales of tens of km or less) has been slow in the decades following Bergeron's work, and major gaps in understanding still persist, particularly with respect to the climatology of precipitation patterns. Progress has been impeded in large part due to insufficient observations of mountain precipitation: gauge networks seldom have the spatial density required to sample subrange-scale variations in precipitation, the distribution of stations tends to be biased towards valley sites (e.g. Groisman and Legates, 1994), and the frozen precipitation often present at high mountain sites is notoriously challenging to measure accurately (e.g. Yang *et al*., 1998). Radar data are also sparse over

mountains due to blocking of the beam by topographic features. Furthermore, only in the past decade or so have observations been augmented with operational numerical weather prediction (NWP) models, run regularly with sufficient spatial resolution to simulate orographic precipitation on scales of 10 km and less (e.g. discussion in Alpert *et al*., 1994).

The distribution of precipitation over mountains is critically important for a range of applications. For instance, landslides and avalanches are triggered by intense and/or persistent precipitation at particular locations within mountainous terrain (Caine, 1980; Conway and Raymond, 1993). The evolution of mountain snow pack, a crucial and changing water resource in regions such as the American West (Mote *et al*., 2005), is also influenced by precipitation distribution. Additionally, the successful prediction of flood events has been shown to be sensitive to the proper simulation of small-scale precipitation features (Westrick and Mass, 2001). Furthermore, if mountain precipitation patterns remain persistently tied to topography over thousands of years, they can be translated into patterns of erosion that shape the mountains themselves, resulting in a coupled co-evolution between precipitation and topography (e.g. Willett, 1999; Roe *et al*., 2002; Stolar *et al*., 2007; Anders *et al*., 2008).

* Correspondence to: Justin R. Minder, Box 351640, University of Washington, Seattle, WA 98195-1640, USA.
E-mail: juminder@atmos.washington.edu

Recently, advances in model resolution, remote sensing, and observations have begun to illuminate the distribution of small-scale orographic precipitation, and the responsible processes. In particular, several field campaigns have produced extremely detailed analyses of individual orographic precipitation events (e.g. the CASCADE (Hobbs, 1975), SCPP (Marwitz, 1987), COAST (Colle and Mass, 1996), MAP (Bougeault *et al.*, 2001), and IMPROVE (Stoelinga *et al.*, 2003) projects), but only recently have small-scale patterns been a focus. Many of these case-studies have involved scenarios with stable flow impinging upon topography, and recent work has shown that small-scale mountain waves, forced by individual ridges, may play a central role in shaping the precipitation distribution. Over the slopes of the Oregon Cascades, airborne dual-Doppler radar data and *in situ* measurements were collected as part of phase 2 of the Improvement of Microphysical Parameterization through Observational Verification Experiment (IMPROVE-2) field campaign. Using these data, Garvert *et al.* (2007) found vertical velocity signatures from gravity waves forced by ∼10 km wide and ∼1 km high ridges and valleys perpendicular to the crest on the windward side of the range during a storm with stably stratified flow. Associated with these waves were enhancements in cloud liquid water, radar reflectivity, and hydrometeor mixing ratios, all centred roughly over the ridges. These anomalies were reproduced in a high-resolution (1.33 km in the horizontal) NWP model, and were found to enhance the precipitation over the windward slope of the range by up to 14%. Colle (2008) looked at the effect of windward ridges on precipitation during stable flow using a NWP model in a two-dimensional, idealized context. He found that for a range of upstream conditions, the addition of ridge-valley relief on the upwind side of a barrier can lead to a local enhancement of precipitation on ridge tops, ranging from 200 to 300%, and a net 10–35% enhancement over the windward slopes as a whole. Similar enhancement of precipitation during stable flow over narrow topographic features has been observed and/or modelled for storms over ridges in the Sierra Nevada (Grubišić *et al.*, 2005), the Mongolian Rim of Arizona (Bruintjes *et al.*, 1994), and the modest hills of Long Island, NY (Colle and Yuter, 2007).

In the presence of unstable impinging flow, stationary and transient convective features triggered by small-scale topography can strongly control the pattern and efficiency of precipitation (e.g. Kirshbaum and Durran, 2004; Fuhrer and Schär, 2005). Such processes represent modes of orographic precipitation which are distinctly different from those found during stable flow. For instance, narrow (2–4 km wide), stationary, connective rain bands have been observed with NEXRAD radar over the coastal mountains of Oregon. These bands of convection are triggered by lee waves associated with ascent over small-scale topographic features, and align themselves parallel to the low-level flow, at times cutting across ridges and valleys (Kirshbaum *et al.*, 2007).

A variety of storms, with varying degrees of stability, were studied during the Mesoscale Alpine Programme (MAP) in the European Alps, and across a range of conditions observations showed precipitation patterns and processes linked to topographic features on scales as small as 10 km (Smith *et al.*, 2003; Rotunno and Houze, 2007). Under conditions with potentially unstable impinging flow, convective cells embedded within stratiform precipitation were associated with intense riming and precipitation over the first narrow range of the Alpine massif (Medina and Houze, 2003; Smith *et al.*, 2003).

The above-noted studies offer detailed accounts of individual storm events, but little is known about storm-to-storm variations in precipitation patterns and how they combine to form a climatological average. Studies which have focused on such issues suggest that small-scale patterns can be pronounced in the climatology and persistent over time-scales of years. Frei and Schär (1998) constructed a gridded precipitation analysis from the dense gauge networks present over the European Alps, and observed ∼40 km scale patterns tied to small ranges. A transect of climatological mean radar reflectivity over the Alps (Houze *et al.*, 2001) shows persistent features on 10 km scales (attributable in part to convection). Anders *et al.* (2006) examined Tropical Rainfall Measuring Mission (TRMM) data, finding 10 km scale precipitation patterns persistent for several years, with major valleys penetrating into the range receiving a great excess of precipitation relative to adjacent ridges. In contrast, Anders *et al.* (2007) found a 60–100% enhancement of precipitation over ∼10 km wide ridges relative to adjacent valleys by analyzing seven years of model output and three years of gauge observations from the Olympic Mountains of Washington State, USA.

While the above studies have demonstrated that small-scale terrain features exert a strong influence on mountain precipitation both for individual storms and in the climatological mean, they also show that the nature of this influence can vary markedly depending upon geographic location and atmospheric conditions. Here we extend the analysis of the small-scale distribution of precipitation over the Olympic Mountains. The availability of long sets of both observational data and NWP output at high spatial resolution allows us to address in detail the following:

1. What are the dominant physical processes responsible for the observed precipitation patterns?
2. How sensitive are the patterns to changes in atmospheric factors such as winds, stability, temperature and frontal regime?

Answers to these questions help extend the understanding of small-scale orographic precipitation in midlatitudes to climatological time-scales. The results have important applications for natural hazards assessments, and ultimately, for the evolution of landscapes over geologic time.

2. Precipitation in the Olympic Mountains

The Olympic Mountains of Washington State, shown in Figure 1, are a roughly dome-shaped coastal mountain range, rising to approximately 2.4 km at the peak of Mount Olympus. The western side of the range, exposed to the prevailing southwesterly winds, receives plentiful annual precipitation (Forks, on the northwestern side of the range receives 3.0 m of annual precipitation), whereas locations in the lee of the mountains are affected by a strong rain shadow (Sequim, on the northeastern side receives 0.4 m annually). The vast majority of the precipitation falls from October to April, within the warm sectors of midlatitude cyclones. (At Forks, for example, only 16% of the annual total falls from May to September). The current stations which report hourly precipitation over the Olympics, shown with stars in Figure 1, are arrayed mainly around the perimeter of the mountains, and are far too sparsely distributed to characterize patterns on a ridge–valley scale. Upper-air conditions are measured via rawindsonde at Quillayute (also indicated in Figure 1) at 00 and 12 UTC.

2.1. Mesoscale modelling over the Olympics

Since 1997 the fifth generation Penn State–National Center for Atmospheric Research Mesoscale model (known as the MM5; Grell *et al.*, 1994) has been run (by the Northwest Regional Modeling Consortium at the University of Washington) at 4 km horizontal resolution over the Pacific Northwest (Mass *et al.*, 2003; http://www.atmos.washington.edu/mm5rt/). The model is run twice daily (initialized at 00 and 12 UTC), forced with initial and lateral boundary conditions supplied by the National Center for Environmental Prediction (NCEP) Global Forecast System (GFS) model. Runs before mid-2002 were forced with the NCEP's 'Eta' model. A variety of changes have been made to the MM5 model grid, initialization, and parametrization schemes since 1997. Most notable for this study are the changes in microphysical scheme from Simple Ice (Dudhia, 1989) to Reisner2 v3.6 (Reisner *et al.*, 1998; Thompson *et al.*, 2004) occurring in February of 2004, and to Reisner2 v3.7 microphysics starting in May 2006. A full listing of model changes can be found at http://www.atmos.washington.edu/mm5rt/log.html

To test for biases in the MM5 simulation of the flow impinging on the western Olympics, we have compared 24-hour model forecasts at 850 hPa to those observed via the Quillayute sounding during conditions characteristic of major precipitation events (flow from the southwest quadrant, 850 hPa wind speeds > 15 m s^{-1}) by calculating the mean error (forecast minus observed) over 203 soundings from two rainy seasons (2005–2006 and 2006–2007). The mean error in the temperature is quite small, $+0.18$ K. MM5 water vapour mixing ratios have a moist error of $+5 \times 10^{-4}$ kg kg^{-1} (about a 12% bias relative to the mean value), but due to documented dry biases in the Vaisala radiosondes (e.g.
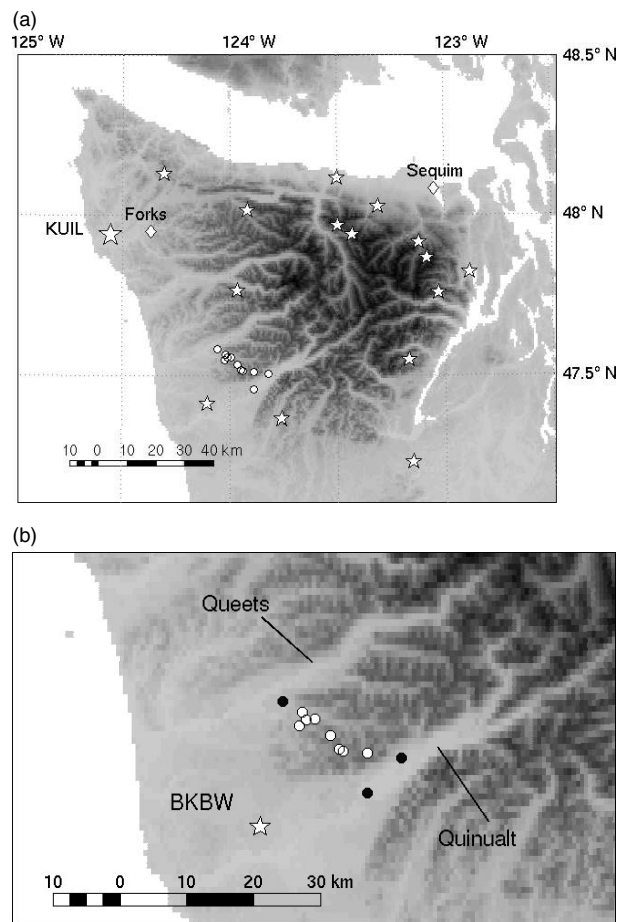

Figure 1. Rainfall observations in the Olympic Mountains. (a) shows the terrain of the Olympic Peninsula (grey shading), with a maximum elevation of 2.43 km. Locations which regularly report hourly precipitation (from the RAWS, ASOS, and the SNOTEL networks) are shown by stars. Locations of the Quillayute (KUIL) sounding, and the COOP stations (Forks and Sequim) discussed in the text are also indicated. (b) shows a detailed view of the Queets–Quinault gauge network. Mixed precipitation gauges are shown by white circles, and rain-only gauges by black circles. The Queets and Quinault Valleys, and the Black Knob (BKBW) RAWS station are also indicated.

Wang *et al.*, 2002) it is unclear if this reflects a deficiency in the model or the observations. The model winds are biased to be somewhat weak and too westerly, with a mean error of -1.1 m s^{-1} (a 5.6% bias relative to the mean) for wind speed and $+8.4°$ for wind direction. Based on the scale of these biases, we expect them to result in only modest errors in the incoming vapour flux available for orographic precipitation. The detailed structures of airflow and precipitation over the Olympics can also be well simulated by MM5, as shown by Colle and Mass (1996) through comparison of airborne radar observations with model output. Results from their work also showed evidence for an enhancement of precipitation over the major ridges on the windward side of the range. Colle *et al.* (2000) compared 1997–1999 cool-season, 4 km MM5 precipitation forecasts to observations and found relatively small biases over the Olympics, which contrasted with significant overprediction of precipitation over the windward slopes of the Cascade mountains.

However, when only heavy precipitation events were considered, a bias towards significant underprediction was observed over the Olympics, with biases approaching 50% at some locations.

The work of Colle *et al.* (2000) also revealed that the climatology of precipitation on the 4 km model domain exhibits significant enhancement over the ∼10 km wide ridges on the windward side of the Olympics. This feature is pronounced, amounting to a 50–300% enhancement on the ridges relative to the valleys, and it has appeared with remarkable consistency in the MM5 annual precipitation totals for over six years (Anders *et al.*, 2007). A climatology of MM5 annual precipitation is shown in Figure 2, for water years 2001–2006. (A water year in this Pacific Northwest is defined to begin on 1 October and end on 30 September. It is designated by the calendar year in which it ends.) This reveals that the modelled ridge–valley pattern of enhancement is not confined to the Olympic Mountains; similar patterns are found over the Cascade, Coastal, and Vancouver Island mountain ranges.

2.2. Queets–Quinault Gauge Network

Motivated by the remarkable ridge–valley precipitation difference in the MM5 forecasts, we established a high-density network of data-logging precipitation gauges in a transect across one of the major ridges in the southwestern Olympics (Figures 1(a,b)). The network of gauges cuts across the topographic ridge that experiences the greatest enhancement of precipitation in the MM5 climatology, from the Queets river valley in the northwest to the Quinault river valley in the southeast. The gauge network has been deployed for water years 2004–2007 during each wet season from early October until late April.
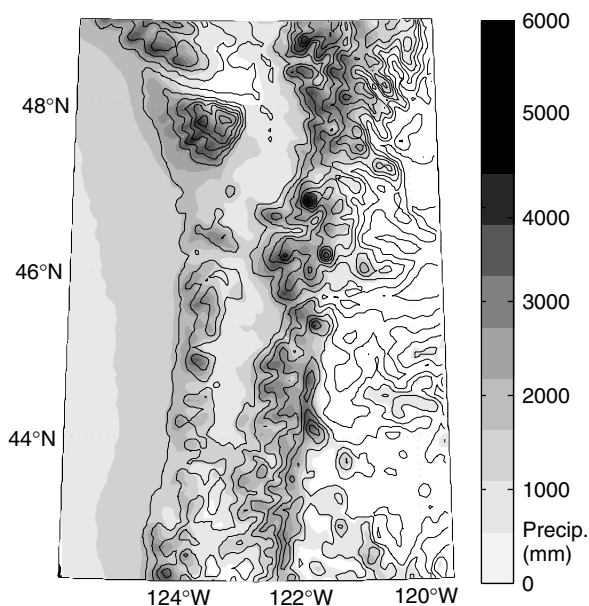

Figure 2. MM5 annual precipitation climatology (water years 2001–2006; shading, mm yr^{-1}), and model topography (contours, interval 250 m) over Olympic, Cascade, and Coastal mountain ranges.

The gauge elevations range from approximately 50 to 900 m. The lowest elevation (< 200 m) gauge sites were equipped with traditional tipping bucket rain gauges with 0.2 mm/tip resolution, whereas higher elevation sites (> 200 m) were equipped with gauges capable of measuring both frozen and liquid precipitation (Figure 1(b)). These mixed precipitation gauges have a resolution of 1 mm/tip, and are similar in design to the gauges described by McCaughey and Farnes (1996) and later produced by Campbell Scientific as snow adaptor CS705. During our field seasons, the percentage of lowland precipitation occurring when the ridge-top temperatures were > 0.5 °C ranged from 74 to 87%, suggesting that much of the precipitation atop the ridge fell as rain. Thus, we do not expect the undercatch of frozen precipitation to introduce large biases into our observations of season-total precipitation. Further discussion of the gauge network can be found in Anders *et al.* (2007).

The incident wind speed and direction influence the pattern and strength of ascent, and hence the resulting pattern of condensation and precipitation (e.g. Hill *et al.*, 1981; Smith and Barstad, 2004). We therefore examine the climatological distribution of winds near our study site. Figure 3(a) is a precipitation-weighted wind rose for the 850 hPa winds from the NCEP–NCAR reanalysis (Kalnay *et al.*, 1996; http://www.cdc.noaa.gov/), weighted by precipitation observations from the Black Knob (BKBW, Figure 1(b)) remote automated weather station (RAWS) – the nearest station to our study area. At 850 hPa, the winds are almost entirely southerly to southwesterly during periods of significant rainfall. A precipitation-weighted wind rose from the 10 m winds measured at BKBW (Figure 3(b)) shows mainly southeasterly to southerly winds during precipitation events. These low-level winds are characteristic of topographic blocking, which occurs when nonlinear dynamics lead to deceleration, and often deflection, of the low-level incident flow (e.g. Pierrehumbert and Wyman, 1985). Thus, from Figure 3, we find that a nearly 90° climatological veering of winds with height occurs during precipitation events, from surface southeasterly winds that are approximately perpendicular to the major subrange-scale topographic ridges and valleys, to 850 hPa southwesterly winds that are parallel to the ridges and valleys. Blocking of low-level flow has been shown to have strong influence on orographic precipitation, both in idealized simulations (e.g. Jiang, 2003), and in observations (e.g. Medina and Houze, 2003), and may be, in part, responsible for the extension of the Olympic mountain precipitation maximum upstream over the coastal lowlands and the Pacific (Figure 2).

We compare the annual precipitation observed by our gauge network with that from the archived 4 km MM5 output by linearly interpolating the 24–36-hour forecasts, summed over entire field seasons, to the gauge locations. MM5 forecast hours 24–36 are used to assure that precipitation has been spun up on the innermost domain (Colle *et al.*, 2000). The apparent long spin-up time on
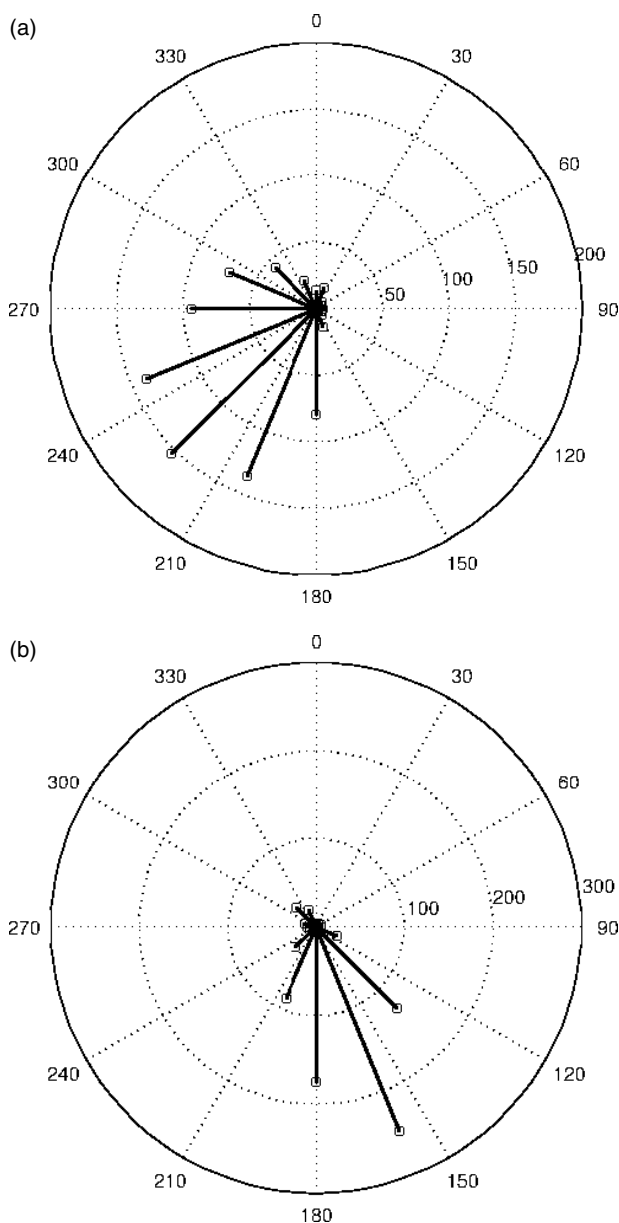
(a)

(b)

Figure 3. Precipitation-weighted wind roses from water years 2004–2006. The length of each radial line is proportional to the amount of precipitation falling at the BKBW station when winds are from that direction. (a) uses 6-hour 850 hPa winds from the gridpoint in the NCEP–NCAR reanalysis upwind of the site during average flow, and (b) uses 6-hour averaged 10 m winds from the BKBW station.

the 4 km domain occurs, in part, because it has been initialized later into the MM5 forecasts, at times which have ranged from hours 6 to 12. The left column in Figure 4 show the field-season totals at each of the continuously operating gauge sites for the past four field-seasons from the MM5 forecasts and the observations. The range of dates defining each field-season are given in Table I. Precipitation totals are plotted as a function of approximate distance along the cross-ridge transect. We find the skill of the model at reproducing the pattern and amount of precipitation at the gauge sites to be remarkable, considering the observational uncertainties associated with the gauging of mixed precipitation, the coarseness of

the model resolution (4 km) relative to the width of the ridge ($\sim$10 km), and the representativeness error associated with interpolating relatively coarsely gridded precipitation fields to point locations (e.g. Tustison *et al.*, 2001). These results affirm that the ridge–valley enhancement is a very consistent and pronounced feature, occurring year after year in both the model and observations.

We consider two measures of the ridge–valley precipitation enhancement:

- R/V: The ratio of the average precipitation at the high-elevation sites (> 200 m) to that measured at the low-elevation sites (< 200 m).
- $R_{\max}/V_{\min}$: The ratio of the maximum precipitation among the high-elevation sites (> 200 m) to the minimum among the low-elevation sites (< 200 m).

The values of these two enhancement metrics for each season are shown in Table I. The same sites are used to calculate the modelled and observed enhancement. However, vandalism and gauge malfunctions disrupted the collection of continuous data at some sites, thus a slightly different network of gauge sites was used for each year (note the different gauge sites shown in Figure 4). Hence, care must be taken in comparing the enhancement between years. On average the MM5 shows a somewhat weaker $R_{\max}/V_{\min}$ enhancement (ranging from 1.45 to 1.60), than the gauges (which range from 1.61 to 1.78). However, even if MM5 were perfectly representing the precipitation processes over the Olympics, we might expect a smaller spatial variability (and hence enhancement) in the interpolated model output solely due to the differences in scale between the point observations of the gauges and the model forecasts of 16 km^2 spatial averages (e.g. Tustison *et al.*, 2001).

For the season totals, the average values of model bias

$$\text{Bias} = \frac{1}{N} \sum_{i=1}^{N} \frac{F_i}{O_i}, \qquad (1)$$

and root-mean-squared error

$$\text{RMSE} = \sqrt{\frac{\sum_{i=1}^{N} (F_i - O_i)^2}{N}}, \qquad (2)$$

are both calculated over the gauge network. F_i and O_i are the forecast and observed precipitation at the ith gauge site, and N is the number of gauge sites. The RMSE values are normalized by dividing by the network averaged precipitation to give a fractional error. These values are shown in Table I. The model does not show a systematic bias towards over- or underprediction of the
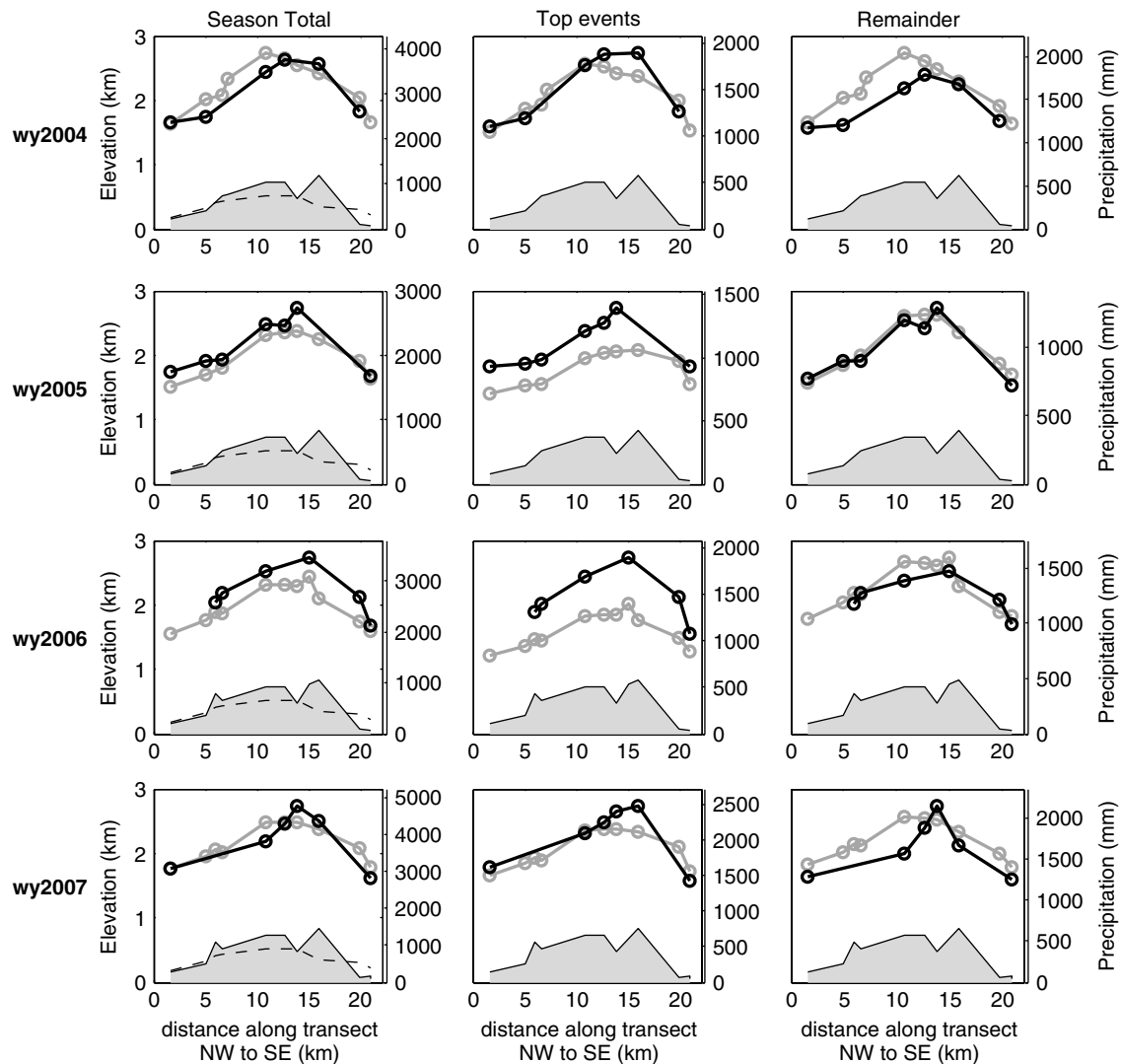
Figure 4. Observed and modelled precipitation totals at sites along the Queets–Quinault gauge transect for four rainy seasons (dates given in Table I). Accumulated precipitation is plotted as a function of approximate distance along the transect. Black lines and circles show observations from the gauges that were continuously operational for the entire season, and grey lines and circles show archived MM5 forecasts interpolated to gauge locations. Elevations of the gauges deployed each year are given by the shaded topographic profile at the bottom of each plot, and the MM5 terrain interpolated to the gauge locations is given by the dashed line in the first column. The columns (left to right) show season total precipitation, precipitation from the largest events, and precipitation from the remaining events; the method for defining events is described in the text. (The use of a different interpolation scheme resulted in somewhat different MM5 values than those shown in Anders *et al.* (2007)).

Table I. Statistics from each observational field season.

Season		wy2004	wy2005	wy2006	wy2007
Dates		17 Oct 2003 −1 May 2004	8 Nov 2004 −4 Apr 2005	10 Oct 2005 −15 Feb 2006	28 Oct 2006 −17 Apr 2007
R/V	Observed	1.40	1.35	1.29	1.57
	MM5	1.48	1.38	1.30	1.37
R_{max}/V_{min}	Observed	1.61	1.61	1.63	1.78
	MM5	1.60	1.59	1.45	1.46
RMSE (normalized)	Season	0.22	0.10	0.11	0.11
	Top events	0.20	0.20	0.26	0.13
Bias	Season	1.16	0.93	0.90	1.04
	Top events	1.08	0.82	0.76	0.97

R/V and R_{max}/V_{min} are measures of ridge-valley enhancement (defined in the text) as observed and modelled (MM5) for the season-total precipitation.
Normalized RMSE and bias of the model forecasts over the network are also defined in the text.

season total, in agreement with the relatively small biases Colle *et al.* (2000) found in the MM5 over the western Olympics for the 1997–1999 rainy seasons.

We have also considered the skill of the model at representing precipitation patterns for individual major storm events appearing in either the gauge observations or MM5 forecasts. We define the top MM5 events by ranking all MM5 24–36-hour precipitation forecasts based upon an areal mean of the accumulated precipitation over the region of our gauge network. We define the top gauged events by ranking our gauge observations based on network-averaged precipitation. The top storm events are formed by separately aggregating the adjacent top MM5 and gauged events into single extended events, and then further combining any extended MM5 and gauge events that overlap. Lastly, the 12-hour periods preceding and succeeding a storm event were also included in that event. This method was chosen to ensure that precipitation events forecast by MM5 with a timing error are compared with the appropriate event in the observations. We define the top storm events to be those storm events which

together make up ~50% of the observed rainfall. The top storm events, chosen in this manner, range in length from 1.5 to 6 days, with a mean length of 2.2 days. The number of top events in a water year varied between 7 and 12.

Figure 5 shows the modelled and observed precipitation for the top events of the water year 2005 field season. Note the large errors apparent for many of the individual events. These storms include events with and without convective instability present in the Quillayute sounding. Also shown are the sum of the top events, the remaining events, and the season total precipitation. The aggregated top events are much better simulated than most of the individual events, and the sum of the many smaller events is simulated even more skilfully. Large model errors for individual storms, contrasting with an excellent modelled climatology, are found for each year (not shown). The sum of the large events and remaining rainfall are plotted in the right two columns of Figure 4. For the large events of water years 2005 and 2006 there is a significant underprediction of precipitation (approaching 25%
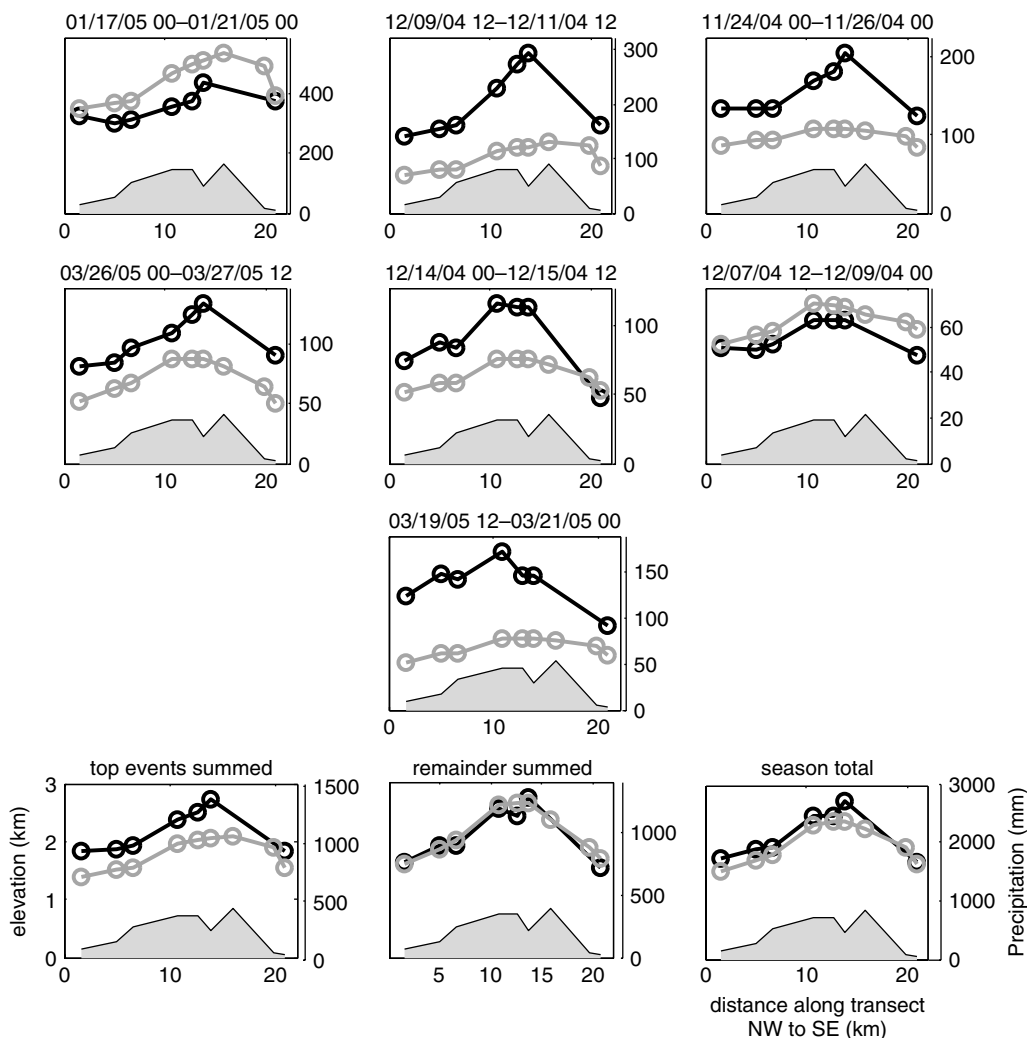

Figure 5. Top rainfall events for the water year 2005 gauge season. The top three rows show the individual top events, determined as described in the text, together responsible for approximately 50% of the observed precipitation during the field season. The bottom row shows the sum of the top events, the sum of the season's remaining precipitation, and the season total. Note that large errors present for individual events show a tendency to average out when events are summed.

for water year 2006) over the region, which is largely masked by the inclusion of the smaller events in the season total. Such underprediction during heavy rainfall is in agreement with the findings of Colle *et al.* (2000) for the rainy seasons of 1997–1999, but does not appear in water years 2004 and 2007. For the remaining smaller rainfall events the model shows little to no systematic bias.

Thus, the integrated effect of a range of over- and underpredicted events is a very realistic model climatology. This suggests that the model is capturing the essential physics controlling precipitation over our study area, however the errors for individual events may be indicative of some deficiency in the model representation of precipitation processes, or the result of random errors. Deficiencies in microphysical parametrizations have been extensively studied as a source of error in the simulation of mountain precipitation (e.g. Stoelinga *et al.*, 2003). Recent work has begun to examine the sensitivity of orographic precipitation forecasts to initial conditions. Walser and Schär (2004) used an ensemble of model runs to show that 'even if the NWP model and synoptic forcing are assumed to be perfect', precipitation forecasts over mountainous terrain may 'on occasions be critically affected by predictability limitations'. Therefore, we hypothesize that errors in the specification of initial conditions (particularly over the observation-sparse Pacific Ocean), may be responsible for some of the large model errors that occur for individual storms.

Lastly, we have also examined the storm-to-storm distribution of enhancements found in the gauge and the model data. For each 00–12 and 12–24 UTC period we calculated the R/V enhancement metric. We consider 12-hour periods where greater than 4 mm of precipitation occurred over our gauge network (since at lower precipitation rates, the ability of our 1 mm/tip gauges to adequately resolve the ridge–valley difference is suspect). We also consider heavy rainfall periods with above 24 mm in 12 hours. As shown in Table II, in the majority of events the ridge–valley enhancement is present. It seems, however, to be a more persistent feature in the model than in the observations. This may point to a real difference between the modelled and actual precipitation patterns during some events. Alternatively, this may be an artifact of observational errors. While snow at the lowland sites is very rare, during cold storms a significant amount of precipitation may fall as snow atop the ridge. Gauges are much more vulnerable to undercatch errors during snowfall (e.g. Yang *et al.*, 1998), so greater undercatch at ridge-top compared to valley sites during cold events may lead to an underestimate of the enhancement for some events in the gauges. Limiting the analysis to periods of heavy rainfall shows the enhancement to be a more persistent feature during such events.

3. Case-studies

The excellent agreement between the modelled and observed precipitation climatology over the Queets–

Table II. Percent of 12-hour periods during each season showing enhanced precipitation (i.e. $R/V > 1$) at the high-elevation (> 200 m) gauge sites relative to the low-elevation (< 200 m) sites, for medium-to-heavy rainfall periods (> 4 mm/12 hrs) and heavy rainfall periods (> 24 mm/12 hrs).

Season	% ridge-enhanced			
	(> 4 mm/12 hrs)		(> 24 mm/12 hrs)	
	Obs.	MM5	Obs.	MM5
wy2004	80	99	91	100
wy2005	94	96	88	100
wy2006	66	92	72	94
wy2007	83	94	91	100

Periods of sub-zero temperatures when one or more gauges were frozen are excluded from the analysis.
The sample size of medium-to-heavy periods ranged from 65 to 199, while the sample size for heavy periods ranged from 11 to 23.

Quinault region, combined with the verification, on 10 km scales, of modelled dynamical and microphysical fields during observing campaigns (Garvert *et al.*, 2007; Colle and Mass, 1996), gives us confidence that MM5 simulations capture the fundamental physical processes responsible for the ridge–valley enhancement over the southwestern Olympics. We have therefore conducted a detailed analysis of several case-studies to diagnose the mechanism for precipitation enhancement in the model and the factors controlling the storm-to-storm variations in the small-scale pattern of precipitation.

Based on archived MM5 forecasts, gauge network observations, and soundings taken from Quillayute, we chose five major precipitation events to simulate, three of which we shall discuss (Table III). In selecting these events we focused upon intense precipitation events, as these matter the most for flooding, landsliding, and erosion. The 28 Nov 2003 and 21 Oct 2003 events contained the largest 12-hour rainfall totals over the network in water year 2004 according to the archived forecasts, and the 17 Jan 2005 event was the largest for water year 2005. We also sampled events with a range of atmospheric conditions to learn if variations in certain atmospheric factors exert significant control on the precipitation pattern. Table III shows the range of stability, wind speeds, wind directions, temperatures, and freezing levels observed during each precipitation event. Lastly, we sought events with atypical precipitation patterns in the gauges and the model, in an effort to better understand the mechanisms that can alter the pattern. The 17 Jan 2005 event had an unusual precipitation pattern with minimal ridge–valley enhancement; storm-total ridge–valley enhancements are also given in Table III.

For each case we have re-run the MM5, with an additional nested 1.33 km resolution domain (not included in the operational runs), so as to better resolve the ridges and valleys of interest. Three microphysical schemes of varying complexity (Reisner2, Simple Ice, and Warm Rain), were used to test the sensitivity of the small-scale patterns

to choice of parametrizations. A complete discussion of the model set-up can be found in the Appendix. We will focus on describing a single canonical example, the 20 Oct 2003 storm, since the basic processes contributing to the pattern were found to be very similar between events. We will then refer to two other case-studies primarily to discuss how variations in the pattern occur.

3.1. Fundamental mechanisms: 20 Oct 2003

On 20 Oct 2003 a surface low tracked up the Pacific Northwest coast, accompanied by heavy rainfall over the Olympics. The 850 hPa heights modelled by the 36 km domain of our MM5 hindcast at the time rainfall commenced are contoured in Figure 6, showing southwesterly flow off of the Pacific impinging upon the Olympics. High surface temperatures (> 10 °C) persisted throughout the storm. Near 19 UTC a second period of heavy rainfall began, with moisture supplied by a relatively narrow band of vapour flux originating in the Tropics which impacted on the Olympics. The feature was simulated by the model, but was displaced to the south, causing the MM5 precipitation to end too early. Thus, we consider only the well-simulated first half of the storm in our analysis.

3.1.1. Comparison of MM5 simulation and observations

Time series of modelled and observed surface variables at BKBW are given in Figure 7 (all model output is from runs using Reisner2 microphysics unless otherwise
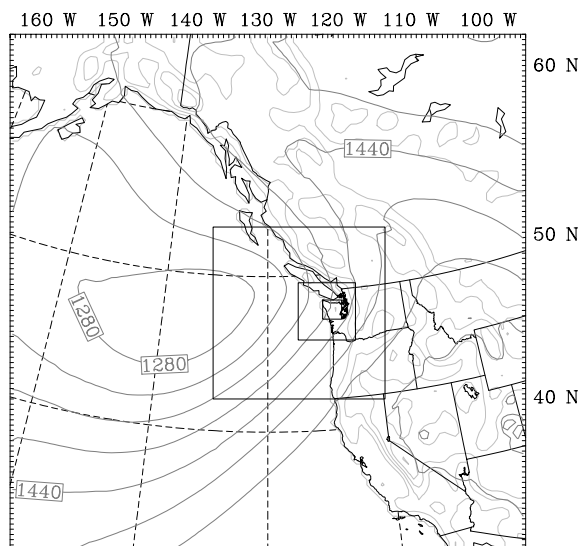

Figure 6. Outermost model domain and large-scale flow for 28 November case-study. The nested MM5 domains (12, 4, and 1.33 km) are shown by boxes. Simulated 850 hPa heights at 12 UTC on 20 Oct 2003 (the time of the beginning of rainfall) are shown by contours (heights are interpolated below the topography in regions of high terrain).

noted). There was a minor timing error in the forecast, thus all MM5 time series are shifted in time by 1 hr so that the changes in rainfall rate match the timing in the observations. Both MM5 and observations show the rainfall occurring within a broad warm frontal zone with rising temperatures and southeasterly flow veering

Table III. Conditions for case-studies discussed in the text.

Case	28 Nov		20 Oct		17 Jan	
Times (UTC) and dates	05Z 28 Nov 2003 −06Z 29 Nov 2003		06Z 20 Oct 2003 −18Z 20 Oct 2003		00Z 17 Jan 2005 −12Z 18 Jan 2005	
	Observed	MM5	Observed	MM5	Observed	MM5
Precip. (mm)	173	131	70	64	241	170
R/V	1.3	1.4	1.6	2.2	1.1	1.3
R_{max}/V_{min}	2.0	1.8	2.6	4.5	1.5	2.8
Temp (°C)	5.6–10.0	4.4–11.7	12.2–15.6	12.8–17.2	9.2–10.6	7.2–12.8
W_{spd} (m s^{-1})	1.8–5.8	2.6–10.3	3.1–7.4	4.1–11.9	3.1–4.5	5.5–7.2
W_{gst} (m s^{-1})	3.6–11.6		5.3–13.8		6.6–9.8	
W_{dir} (deg.)	130–340	140–320	120–190	100–210	187–240	210–171
FL (km)		1.0–3.0		2.5–3.8		2.2–3.1
$N^2_{m(0-2km)}(\times 10^{-5}$ s$^{-2})$		2.5–15.0		−10.0–7.3		2.3–11.0
$W_{spd(0-2km)}$ (m s^{-1})		6–32		11–32		11–28
$W_{dir(0-2km)}$(deg.)		173–316		157–213		173–244

Observed and modelled (MM5) surface conditions:
Precip. gives the storm-total precipitation at the BKBW station.
R/V and R_{max}/V_{min} give the ridge-valley enhancement as described in the text.
Temp, W_{spd}, W_{dir} denote the ranges of 2 m temperature, and 10 m wind speed and direction at BKBW.
W_{gst} denotes the range of observed wind gusts.
Metrics from the modelled KUIL sounding:
FL gives the range of freezing levels.
$N^2_{m(0-2km)}$, $W_{spd(0-2km)}$, and $W_{dir(0-2km)}$ give the ranges of moist static stability, wind speed, and wind direction averaged between 0 and 2 km.

to southerly with time. The model represents well the changes in wind direction and temperature that occur over the course of the event, although the simulated surface windspeeds are closer to the observed gusts than the observed sustained winds. One-hour average precipitation rates for ridge and valley sites are shown in Figure 7(a). Peak 1-hour averaged rainfall rates in the model and gauges exceeded 16 mm hr^{-1}, and rates greater than 8 mm hr^{-1} were sustained for over 5 hours. The overall duration and intensity of the event are well modelled. Both observations and the model show a ridge-top enhancement of precipitation throughout the event and the magnitude of the enhancement is well simulated during the periods of significant rainfall.

The 12 UTC 20 Oct 2003 sounding at Quillayute (black line in Figure 8) gives a profile of conditions upwind of the mountains at the beginning of the heavy rainfall. Very strong low-level winds were observed, veering with height (as expected in the pre-frontal region of warm advection) from south to southeast near the surface to southwest around 800 hPa. Near-neutral stratification was present throughout much of the sounding. However, a stable layer occurred between 900 and 800 hPa associated with the warm-frontal zone aloft, and was capped by a slightly unstable layer (with respect to saturated vertical displacements). The freezing level at

this time was above the topography, near 625 hPa. The model sounding (shown in grey, shifted 1 hour in time as for Figure 7) captures the basic vertical structure well, but the MM5 exhibits an upward displacement of the warm front, and lacks the unstable layer.

The simulated storm-total (06–18 UTC on 20 Oct) pattern of precipitation is shown in Figure 9(a). The same pattern of enhancement found in the archived 4 km MM5 climatology (i.e. Figure 2) is reproduced for this case. Ridge–valley enhancement during this case was particularly strong: within the Queets river valley storm total precipitation was as low as 30 mm, whereas a few km to the southeast, atop the adjacent ridge, precipitation totals exceed 160 mm.

In Figure 9(b), observed and modelled storm total precipitation at our gauge sites are plotted. Totals are shown from the 1.33 km domain of our MM5 Reisner2 hindcast, as well as the 4 km domain, and for runs of using less sophisticated microphysical schemes, allowing us to assess the impact of changes in horizontal resolution and physical parametrization on the simulation. All these simulations capture the basic shape and magnitude of the enhancement. However, the location of the observed precipitation maximum is shifted upwind over the first prominent peak on the southwest side of the ridge, whereas, the modelled precipitation is centred over the
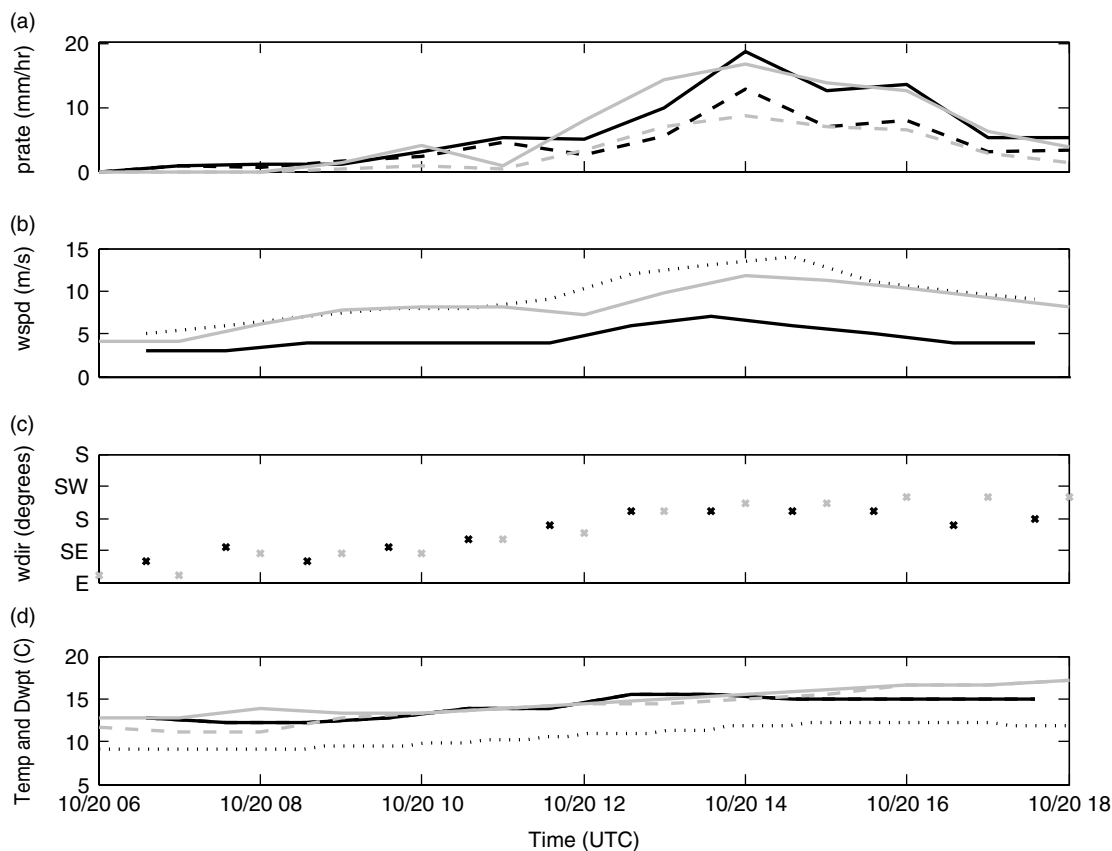

Figure 7. Modelled and observed time series from the 20 Oct 2003 storm. Black lines and points show observations, while grey lines and points show MM5 hindcast. (a) 1-hour precipitation totals at gauge network sites. Solid lines are for the average of all high elevation sites (> 200 m), while dashed lines are for low elevations (< 200 m). (b) Modelled and observed wind speed (solid) and observed wind gusts (dotted) at BKBW station. (c) Wind direction. (d) Temperature (solid) and dew-point (dashed) at BKBW, and temperature at ridge-top site (dotted). Note that observations show fully saturated conditions throughout the period, and hence the dewpoint is plotted atop the temperature and not visible.
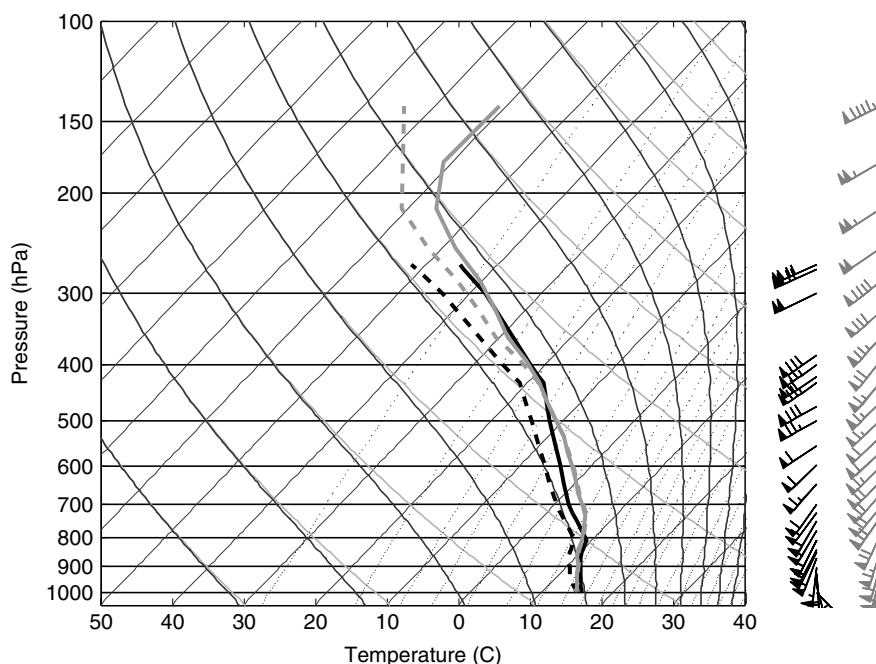
Figure 8. Skew$T$–log$p$ plots of observed and modelled soundings at KUIL at 12 UTC, 20 Oct 2003. The observed sounding is shown in black (temperature solid, dew point dashed). A profile of winds is shown on the right, with each full barb representing 5 m s^{-1}. The model sounding is shown in grey, and is taken 1 hour prior to the observation time to account for the error in the model timing of the storm passage.

crest. Overprediction of cross-ridge winds (Figure 7) may have contributed to this error in location of the modelled maximum by the excess downwind advection of falling rain. The simulations with various microphysical schemes show only minor differences in precipitation over the ridge, with the intermediate complexity scheme (Simple Ice) producing the most skilful representation of the rainfall totals. The insensitivity to choice of parametrization for this storm is perhaps unsurprising, considering the high freezing level, which implies the dominance of warm microphysical processes (which are represented quite similarly between the considered schemes). For this case, and the cases in the following two subsections, the GFS (spectral resolution T254)-driven operational forecast (not shown) exhibited similar errors to our reanalysis (spectral resolution T62)-driven hindcasts, suggesting that the relatively coarse resolution of our initialization and boundary grids was not the major source of forecast error.

3.1.2. Mechanism for precipitation enhancement

Having gained confidence that the MM5 is faithfully representing the basic characteristics of this event, we now proceed to investigate the mechanisms responsible for the ridge–valley enhancement in the model. We will focus upon the time of heaviest precipitation in the model (forecast hour 27, or 14 UTC on 20 Oct). Shown in Figure 10(a) is the 1-hour precipitation total over the western Olympics for the hour previous to this time, as well as the 10 m modelled winds. Low-level winds are southerly and impinge obliquely upon the northeast–southwest oriented ridges. Figures 10(b–d)

show vertical cross-sections taken parallel to the low-level winds across the ridge from north to south. Figure 10(b) shows contours of precipitation rates (i.e. vertical flux of precipitation) for the modelled species of hydrometeors. The majority of the enhancement in the precipitation rate over the ridges takes place at low levels, with much of it occurring in the rain water field at less than 1 km above the ridge crest. A signature of the enhancement is also found higher up, above the freezing level, in the graupel and snow fields.

Vertical velocity and cloud water mixing ratio are plotted along the transect in Figure 10(c). Strong ascent (descent), exceeding 2 m s^{-1}, is found over the windward (leeward) slopes, extending up to 4 km elevation, with indication of a slight upstream tilt with height of the vertical velocity fields. Such patterns of vertical motion are expected from the theory of mountain waves in stably stratified flow (e.g. Smith, 1979). The cloud water field shows an intense maximum (> 0.75 g kg^{-1}) located between the maximum and the node in the vertical velocity. The presence of this dense cloud is due to the ascent in the mountain wave, but its downwind displacement from the location of maximum vertical velocity, and its detailed structure, are set by the balance of condensation, downwind advection, and loss of cloud water due to precipitation (e.g. Smith and Barstad, 2004).

To understand the pathways by which condensed water over the ridges is converted into precipitation we examined the source terms for precipitation in the Reisner2 microphysical scheme. We focus on the conversion terms in the scheme that create precipitation, and not those which transfer water between the various species of hydrometeors. We average these terms over the windward
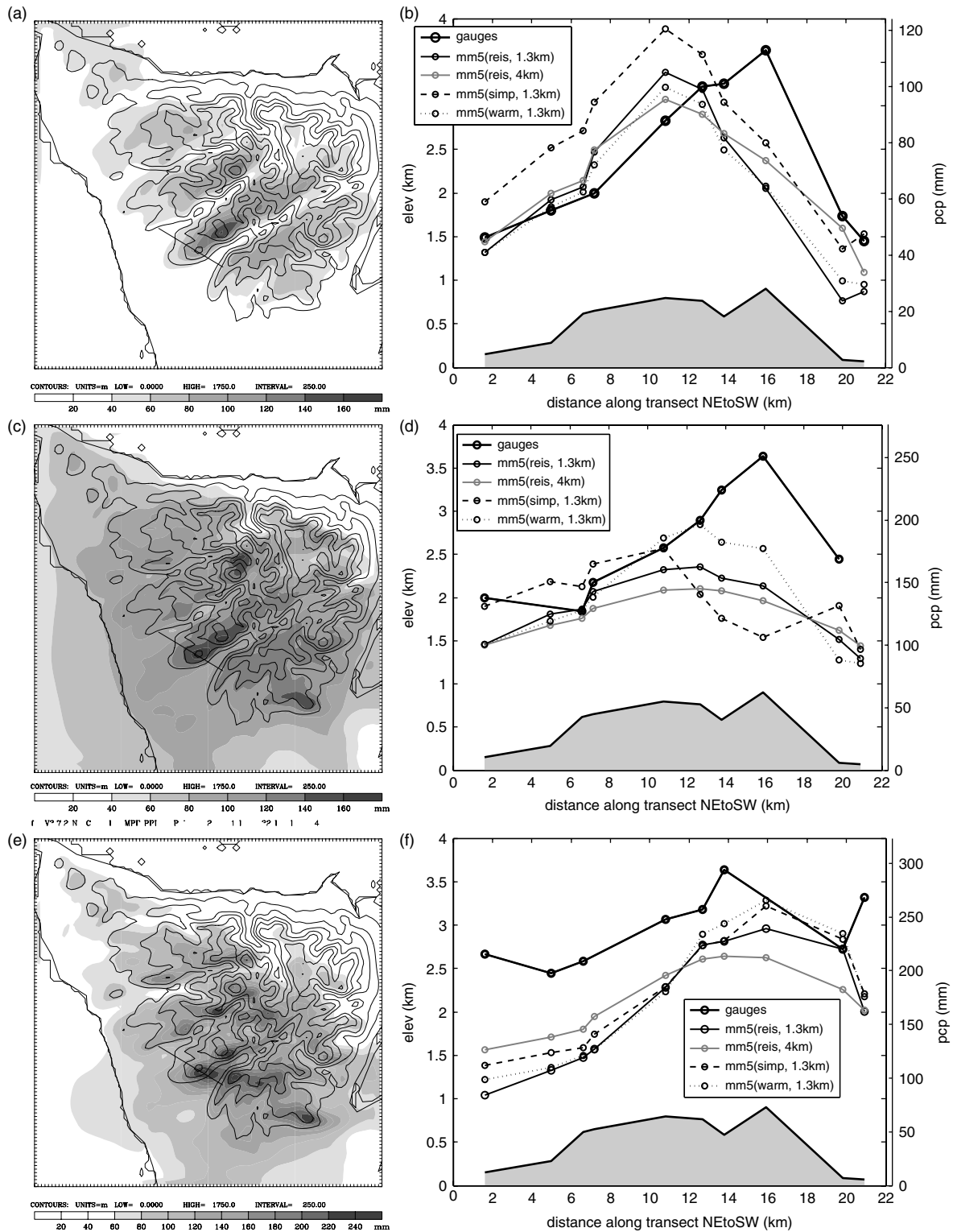
Figure 9. Storm total precipitation for case-studies. (a) Storm total precipitation (shading) for 20 Oct 2003 event as modelled by MM5 with 1.33 km horizontal resolution and Reisner2 microphysics. Tick marks along the perimeter of the map show the model grid spacing. (b) Observed and modelled precipitation at gauge network sites as a function of distance along the transect. Observations are shown by the bold black line; output from MM5 simulations with varied resolution and microphysical parametrizations are shown as in the legend. The elevation of gauge sites is represented by the shaded terrain profile. (c) and (d) are as (a) and (b) but for the 28 Nov event. (e) and (f) are as (a) and (b) but for the 17 Jan event. The time intervals used for the storm total transects and maps are given in Table III.

slopes of the Olympics for this time, from the surface to 200 hPa, using the methods described by Colle *et al.* (2005). This analysis shows that about eight times more

water vapour is condensed into cloud liquid water than is deposited onto ice particles, underscoring the importance of liquid phase microphysics for this event. Furthermore,
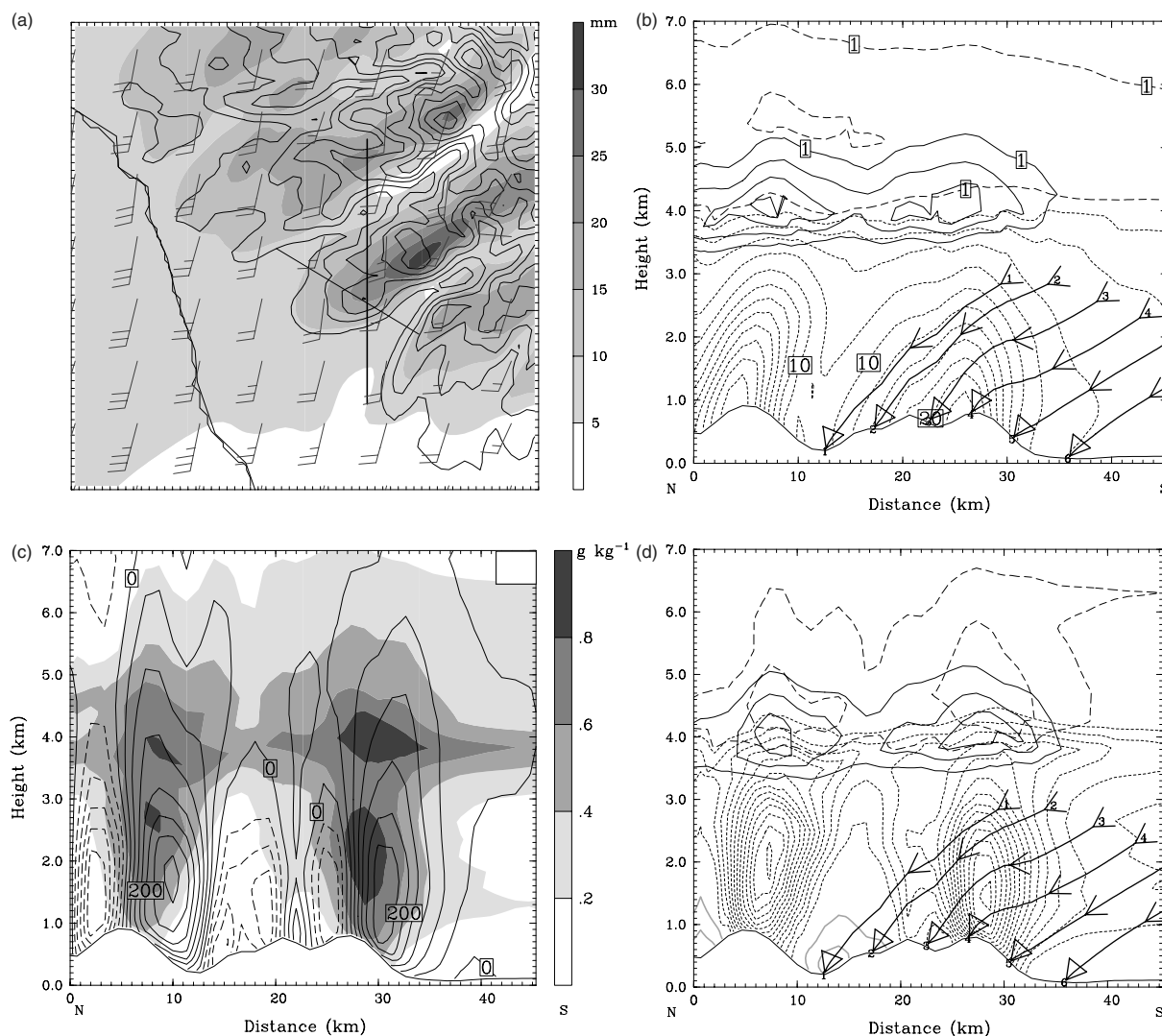
Figure 10. Precipitation patterns and processes at time of peak modelled rainfall (14 UTC on 20 Oct 2003). (a) Map view of 1-hour accumulated precipitation (grey shading), with elevation (contours, 200 m interval), and 10 m winds (wind barbs, full barb = 10 kts). Location of the gauge network (thin NW–SE line), and the following cross-sections (bold N–S line) are also shown. (b) Vertical cross-section parallel to near-surface winds, precipitation rates are contoured for rain (fine dashes) every 2 mm hr^{-1}, and for graupel (solid) and snow (long dashes) every 1 mm hr^{-1}. (c) Cloud water mixing ratio (grey shading, scale shown on the right), and vertical velocity (contours at interval 40 cm s^{-1}, with negative values denoted by dashed contours). (d) Contours of Reisner2 precipitation source terms including the collection of cloud water by rain (fine dashes), graupel (solid black), and snow (medium dashes), and the sink of precipitation by evaporation (solid grey), all at intervals of 2.5×10^7 s^{-1}. Characteristic hydrometeor back-trajectories (as described in the text) are shown as bold black lines and arrows in (b) and (d).

the largest sources of precipitation, by at least an order of magnitude, are found in the terms involving collection of cloud liquid water. These include the collection of cloud water by rain, graupel, and snow (contoured in Figure 10(d)). All of these terms have maxima in the regions of thick cloud and intense rain over the ridge, and the largest source by far is the collection of cloud water by rain, maximizing at low levels. For this case, evaporation of rain within the sub-saturated valleys appears to also make a contribution towards the ridge–valley precipitation differential (grey contours in Figure 10(d)), but this effect was modest and was not observed in other cases. Thus, low-level collection of cloud droplets in wave-induced clouds appears to be the dominant control on the ridge–valley precipitation pattern during this storm, whereas auto-conversion of cloud

water, depositional growth of snow, and evaporation of rain in sub-saturated valleys have relatively minor roles in directly determining the rainfall distribution.

The downwind drift of precipitation can play a key role in determining the rainfall pattern (e.g. Hobbs *et al.*, 1973). To illuminate this effect we determine characteristic back-trajectories of hydrometeors that land at various locations along the cross-section (Figures 10(b,d)). These trajectories are calculated using the mass-weighted fall speed of hydrometeors as represented in the microphysical scheme, as well as the model fields of horizontal and vertical motion. The trajectories are integrated back in time with a time step of 10 s, using winds interpolated from the hourly model output (we justify the use of hourly winds by the steadiness of the modelled winds at this time). The plotted trajectories trace the path of

hydrometeors back 10 minutes in time, with the middle arrow head showing the position at 5 minutes. From these plots we see that trajectories ending on the ridges (in the valleys) where rainfall rates are high (low), spend the longest (shortest) period of time in the region of thick cloud and extensive collection. Downwind drift spreads the enhanced precipitation beyond the region of enhanced condensation and collection. For instance at 17.5 km along the transect high precipitation rates are found, despite relatively modest cloud water mixing ratio and collection sources overhead, since the trajectory ending there passes through the region of enhanced collection.

Since condensation in the ascending branch of the ridge-induced mountain wave is the source of the enhanced precipitation, it is important to understand the wave structure. Figure 10(c) shows the mountain waves signature over the ridges decays near 3–4 km. A model sounding upstream of the ridge at 14 UTC shows average low-level (surface to 1 km) stability (moist buoyancy frequency) of 0.008 s^{-1} (using Equation 36 of Durran and Klemp (1982)) and cross-ridge wind speed of 15 m s^{-1}. If we idealize the impinging flow as uniform and two-dimensional, linear mountain wave theory (e.g. Smith, 1979) would predict that, under these conditions, 20 km wide undulations in the topography would produce mountain waves that would propagate vertically, whereas waves forced by 10 km undulations would decay with a vertical scale of 3.0 km. Thus for this case, the waves triggered over the major ridges are near the limit for vertical propagation, so decay of the waves is not entirely surprising. In contrast, during the 28 Nov case, waves are observed at times when linear theory (with uniform impinging flow) predicts propagation even for 10 km-scale waves, and model output shows notable upstream tilt suggesting that the waves are indeed propagating, nonetheless model output shows them decaying near 3 km.

Therefore, simple (2D, uniform impinging flow) linear theory predicts the presence of standing waves rising above the major ridges of the Olympics, but not always the decay of these structures which is simulated in MM5. The vertical structure of the impinging flow offers two explanations why waves might decay even when simple linear theory predicts propagation. Figures 11(b,d) show vertical cross-sections of the flow, taken perpendicular to the ridge, with contours of vertical velocity and equivalent potential temperature, θ_e, as well as velocity vectors in the plane of the cross-section. The θ_e lines coincide with stream lines for moist pseudo-adiabatic flow, and their vertical spacing is a rough indicator of moist stability. Decay of the waves in the vertical velocity field occurs near the height where the θ_e lines become much more widely spaced, above the warm frontal boundary. The drop in stability which this implies represents a change in the propagation characteristics of the atmosphere (namely the index of refraction of the gravity waves), which may cause a vertically propagating wave to become evanescent and decay with height (e.g.

Smith, 1979). But directional shear in the profile of impinging winds also occurs near this height (associated with the warm advection beneath the front), forming a directional critical layer where the winds become parallel to the phase lines of the waves forced by the topography. Gravity waves are unable to propagate through such a level as their energy is absorbed or advected downstream (Shutts, 1998; Doyle and Jiang, 2006). Figures 11(a,c) show the 1 km and 3 km winds. As expected from the theory of critical levels, the height at which the mountain wave vertical motions decay to near-zero coincides with the height at which the cross-ridge winds become negligible due to the veering with height. Examining the time evolution of the wind and stability profiles and wave structure throughout this and other simulated storms reveals that the vertical extent of the mountain wave co-varies with the height of the warm front aloft, however it is unclear if this is due to the changes in wind direction or stability across the front.

While the above-described mechanisms are the predominate control on the rainfall distribution for each case, distinctly different patterns and processes dominated during a few periods of our case-studies. These departures are interesting in that they lend insight into which processes can lead to an unexpected rainfall pattern, and may be the rule rather than the exception either in other geographical regions or in past or future climates. We will explore the two principal exceptions we encountered in the following two subsections.

3.2. Influence of the freezing level: 28 Nov 2003

The synoptic forcing leading to the 28 Nov 2003 event included the passage of a mature surface low pressure centre to the north of the Olympic peninsula. Heavy precipitation (> 10 mm hr^{-1}) occurred throughout an 8-hour period of warm advection and rainfall quickly dropped off after a cold-frontal passage. Both observations and model output of storm-total precipitation for this event, shown in Figure 9, show enhancement over the ridge, however the enhancement is not as strong or well-simulated as in the 20 Oct case. There was a timing error in the simulation of the storm, so all model output has been shifted forward in time by 6 hours.

Throughout the main portion of the storm, steady mountain waves occurred over the ridges and the mechanisms discussed for the 20 Oct storm dominated the precipitation pattern. However, early in the storm a distinctly different precipitation pattern occurred, which is masked in the storm total by the more voluminous rainfall that followed.

During the beginning of the 28 Nov event (05–14 UTC), observed ridge-top temperatures were near freezing, and the modelled KUIL soundings showed a low freezing level (near 800 hPa). The MM5 matches the basic structure of the 12 UTC Nov 28 KUIL sounding, but underpredicts the freezing level by over 1 km (since it misforecast the altitude of the front aloft). During the hours immediately before and after the sounding the
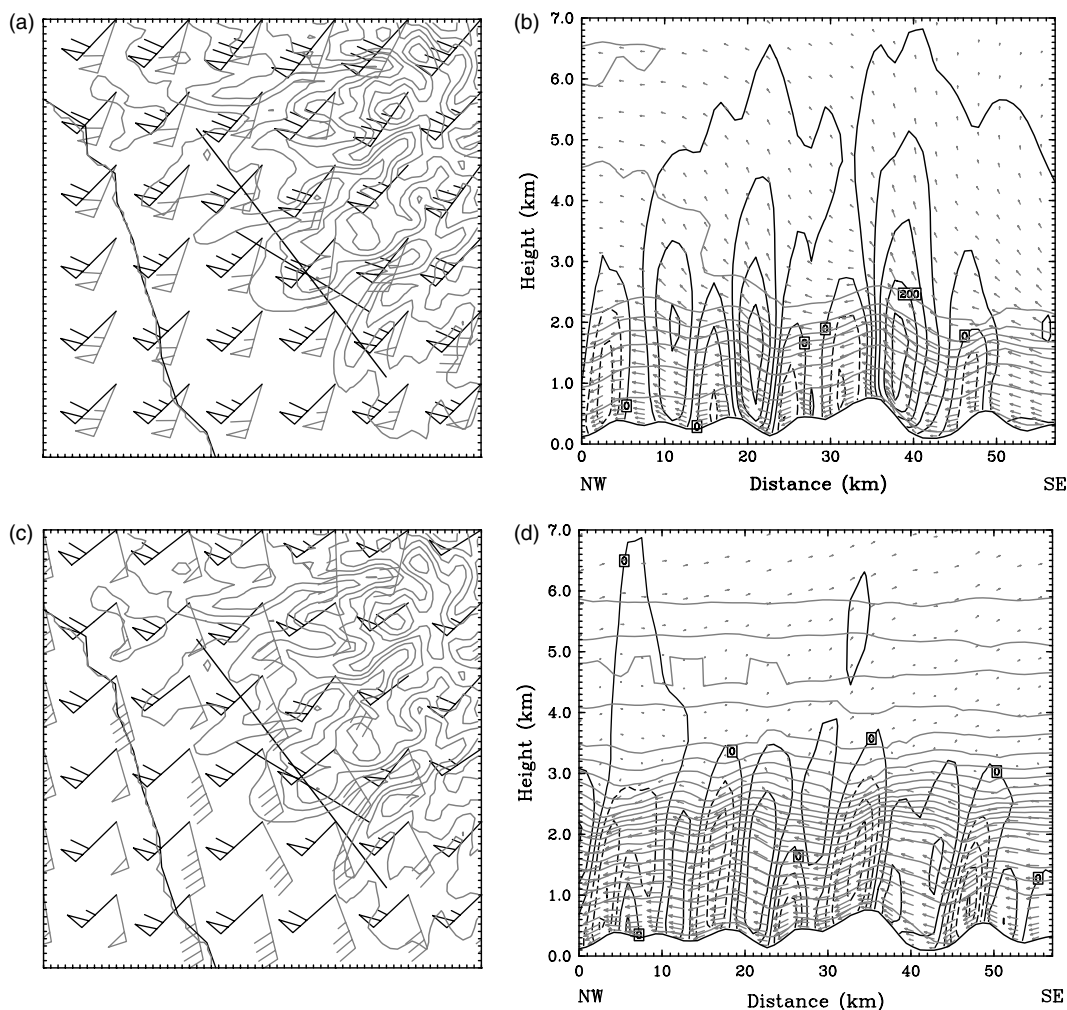
Figure 11. Wave structure, stability and directional critical level. (a) Winds at time of maximum rainfall (14 UTC) for the 20 Oct case are shown with barbs at 1 km (grey) and 3 km (black) (full barb = 10 kts). (b) Cross-section (at location of bold line in (a)) of vertical velocities, and cross-ridge circulation. Contours of equivalent potential temperature are also shown (light grey lines, at intervals of 1.5 K). Note that the mountain wave decays as it passes through the warm front aloft, where the stability drops and the cross-ridge component of the wind approaches zero. (c) and (d) are as (a) and (b), but for a time during the 28 Nov case.

MM5 significantly underpredicts the precipitation rates at high elevation sites. This may be due to the low simulated freezing level which could have led to excess advection of snow into the lee. Nevertheless, during the earliest hours of the storm (06–10 UTC), observations and the simulation agree better and both show an atypical pattern of precipitation. Figure 12(a) shows a map of simulated precipitation totals over the Olympics during this period. Precipitation does not maximize on the crests of the southwestern Olympic ridges, but rather over their lee slopes (the wind being from the southsoutheast). The transect in Figure 12b shows that while the details of the precipitation distribution are not all captured by the MM5 Reisner2 run, both model and the gauges portray a pronounced maximum shifted away from the ridge crest into the lee.

Due to the much slower fall speed of snow compared to rain, periods with low freezing level and strong cross-barrier flow can be associated with enhanced spillover of orographic precipitation onto lee slopes (e.g. Sinclair *et al.*, 1997). Figure 13(a) shows a cross-section

of cloud water, precipitation source terms, and hydrometeor back-trajectories analogous to Figure 10(d). The hydrometeor trajectories shown are significantly shallower than those depicted in Figure 10(d) (as well as those simulated during the peak of the 28 Nov rainfall), and trajectories ending in the lee valley pass through the region of enhancement while those ending on the windward slope do not, suggesting that advection of slow falling snow into the lee is responsible for the abnormal pattern. The exaggeration of the lee maxima in the Simple Ice run (Figure 12(b)) is consistent with previous results showing that the scheme advects too much precipitation (in the form of snow) onto the lee slopes due to the neglect of supercooled water and faster-falling graupel (e.g. Colle *et al.*, 2005). The more typical ridge-top enhancement pattern found in the Warm Rain simulation supports the notion that the lee-side maxima is due to processes involving frozen hydrometeors. Our findings are in agreement with those of Zängl (2007), who presented observations of enhancement in the lee of narrow mountains in the Alps during storms with low freezing
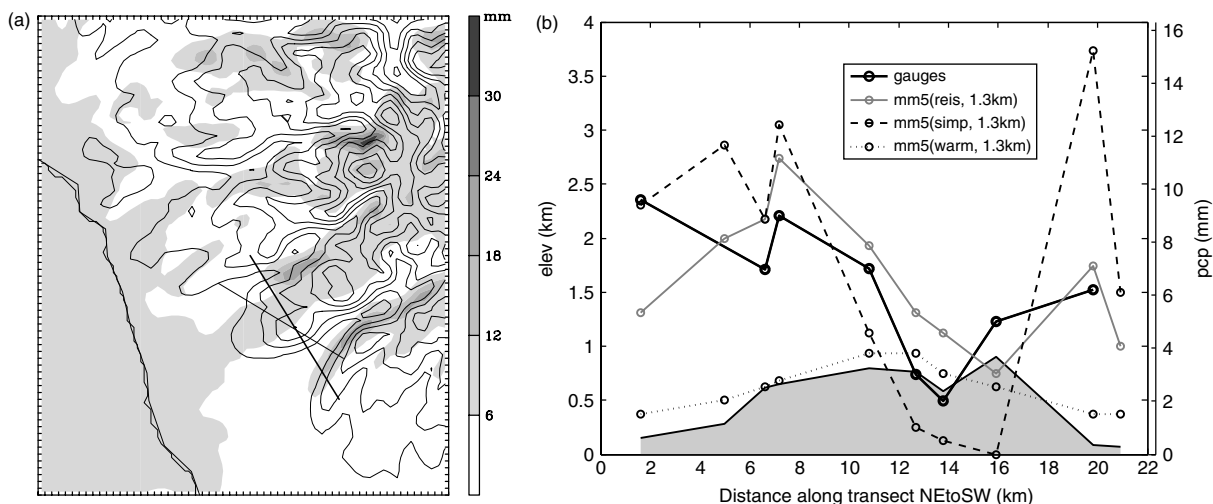
Figure 12. Modelled and observed rainfall distribution for the early portion of 28 Nov storm, with low freezing level. (a) Accumulated precipitation over western Olympic Mountains between 05 and 10 UTC in MM5 1.33 km simulation with Reisner2 microphysics. (b) Accumulated precipitation for the same period as in (a) for sites along the gauge transect, from observations and 1.33 km MM5 domain for different microphysical parametrizations.
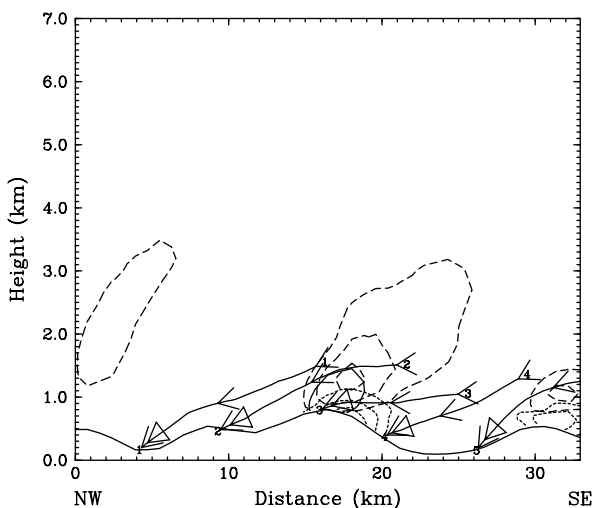

Figure 13. Cross-section of modelled precipitation sources (contours, with interval 1×10^7 s^{-1}) and trajectories at 10 UTC on 28 Nov 2003. The section is taken parallel to the low-level flow (along bold line shown in Figure 12). Plotting conventions are as in Figure 10(d). Note the shallower slopes of the hydrometeor trajectories than those in Figure 10(d).

levels. His simulations of these Alpine storms suggest that when the freezing level is located near the crest of a narrow mountain, lee-side enhancement is produced via a combination of downwind advection of frozen hydrometeors generated in the orographic cloud, and by the flux of frozen hydrometeors through the freezing level associated with mountain wave descent.

3.3. Influence of convection: 17 Jan 2005

The 17 Jan event was part of a prolonged period of several days of heavy rains that occurred as a mid-level short wave passed, and a low-level baroclinic zone was maintained over the region. There was no passage of distinct surface fronts during this case, only a diffuse frontal zone of warm advection. As with the 20 Oct case, the freezing level remained more than 1 km above the ridges. Early in the storm, collection in stable orographic clouds over the ridges dominated the rainfall pattern as detailed for the 20 Oct event. Near 17 UTC on 17 Jan, a transition to unstable conditions occurred. The MM5 accumulated precipitation for this event showed a typical pattern of ridge-crest enhancement over the northernmost ridges of the western Olympics, but an atypical valley maxima over the Quinault valley (Figure 9(e)). The transect of gauge observations (Figure 9(f)) also shows some indication of a valley maximum, in addition to a subdued maximum over the crest.

Near 18 UTC on 17 Jan 2005, both observed and simulated soundings from KUIL showed a transition from stable/neutral to neutral/unstable conditions at low-to-middle levels (the simulated squared moist buoyancy frequency between 1 and 3 km (Durran and Klemp, 1982) changed from 8.7×10^{-5} s^{-2} at 14 UTC to -3.9×10^{-5} s^{-2} at 22 UTC). Accompanying this was the disappearance of the steady waves of cloudwater and vertical motion over the ridges, and the appearance of individual transient cells of which began precipitating offshore and were advected across the mountains (apparent in 10-minute model output (not shown)). These features consisted of elevated cores of upward motion, with flanks of subsidence, indicative of cellular convection. The precipitation rates associated with these features more than doubled as they encountered the topographic barriers of the Olympics.

Simulated precipitation totals from before and after the transition to unstable conditions are depicted in Figures 14(a,c). After the transition to cellular convection, the pattern of rainfall over the region of our field study was less tightly tied to the topography, and included a rainfall maximum in the Quinault valley which occurred
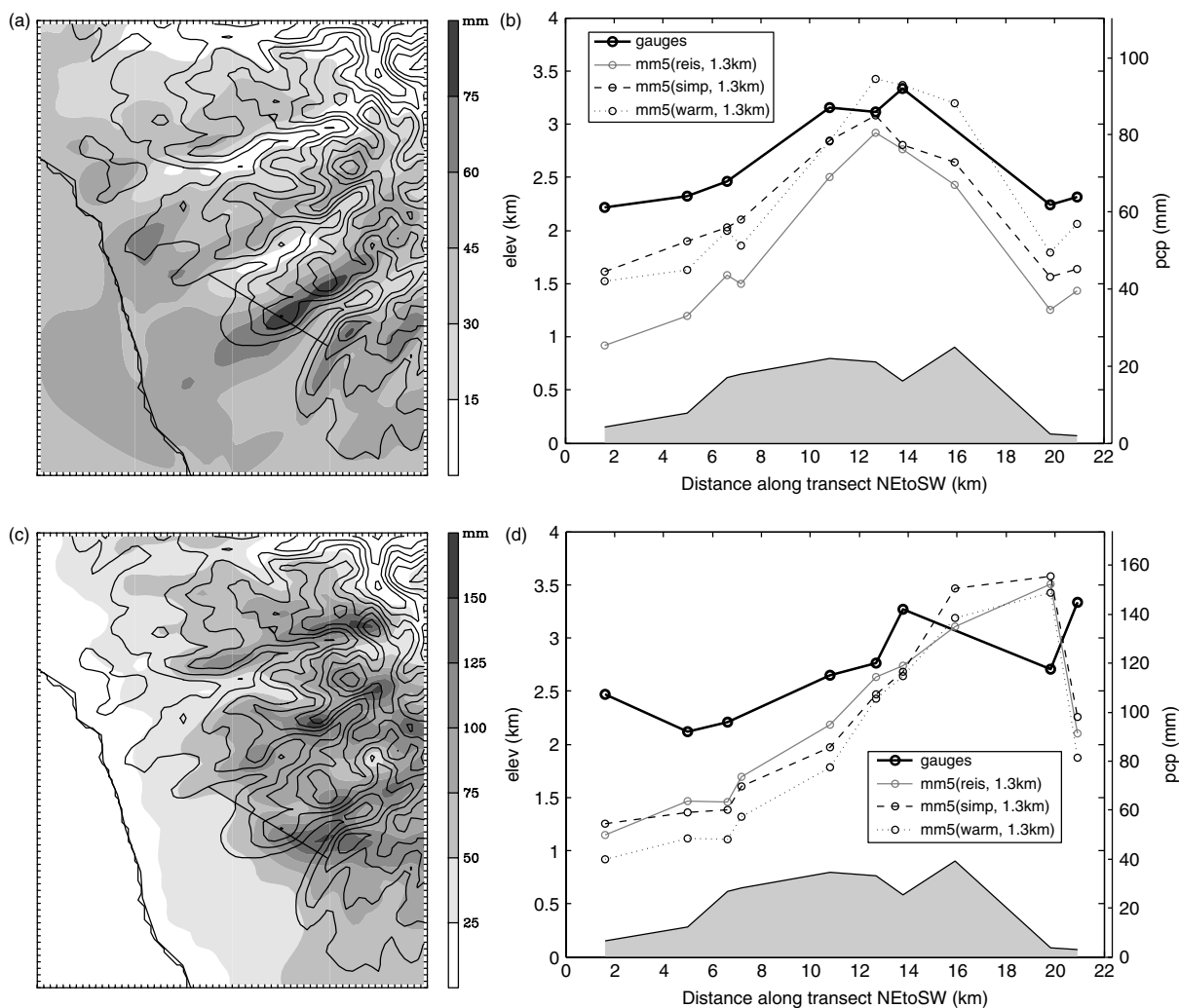
Figure 14. Modelled and observed rainfall distribution for stable and unstable portions of the 17 Jan storm. (a) shows accumulated precipitation simulated over western Olympic Mountains between 00 and 16 UTC on 17 Jan 2005 (stable period). (b) Precipitation for sites along the gauge transect from observations and 1.33 km MM5 domain using different microphysical parametrization during same period as (a). (c) Shows accumulated precipitation simulated between 22 UTC on 17 Jan and 12 UTC on 18 Jan (convective period). (d) Precipitation for sites along the gauge transect from observations and 1.33 km MM5 during same period as (c).

as a result of transient cells which tracked over the valley. Channelling of flow into the valley did not appear to play a role. Gauge observations also exhibit an abnormal pattern during this period, with a valley rainfall maximum, in contrast to the more typical ridge-top maximum seen in the earlier portion of the storm (Figure 14(b)). These results suggest that during times of convection, the absence of mountain-wave-generated cloud water over topographic ridges and the scattered tracks of individual convective cells may lead to precipitation patterns which are fundamentally distinct from typical storm totals and the climatological mean.

Stationary bands of of convection were briefly simulated late in the 20 Oct case (not shown). Like those examined by Kirshbaum *et al.* (2007), these rainbands were only a few km wide, triggered over topography, and aligned parallel to the low-level flow. These bands were not modelled on the 4 km domain, as they were too small to be resolved by such a grid; thus they represent a feature of mountain precipitation not captured

by the operational forecasts, and may account for some of the discrepancies between the models and observations. However, the excellent agreement between the 4 km MM5 and our gauge network over the western Olympics suggests that, at least in that region, such banded convection is not a dominant mechanism shaping the precipitation climatology.

4. Composite analysis of precipitation climatology

The above-analyzed case-studies yield suggestions as to the importance of various atmospheric factors in controlling the small-scale distribution and enhancement of mountain precipitation. For instance, changes in wind direction during the course of storm events (e.g. those shown in Figure 7) did not result in noteworthy changes in the spatial structure of precipitation, whereas changes in the height of the freezing level appeared to drastically reshape the pattern.

We have already shown that the pattern of ridge–valley enhancement found in our case-studies dominates for the majority of storms and in the climatological mean. We now use our gauge observations and the archived MM5 forecasts to test hypotheses about what factors are responsible for variations in the ridge–valley precipitation pattern. To do so we composite rainfall totals at sites within our field study area based upon upwind atmospheric conditions.

Figure 15 shows 12-hour accumulated precipitation, composited based upon 12-hour averaged 2 m temperatures measured at BKBW, as a function of distance along the gauge transect for the water year 2006 field season. For high temperatures ($> 5\,°C$), the enhancement of rainfall over the ridge is pronounced. However, for lower temperatures, the ridge–valley enhancement is minimal. Each year of gauge data was analyzed separately, since very few gauges were continuously operational for the full duration of all four field seasons. However, similar results of reduced enhancement at low temperatures were found for all but one field seasons (water year 2005). This relationship between surface temperature and enhancement could be associated with changes in the height of the freezing level, and downwind drift of frozen hydrometeors as discussed in section 3.2.

Alternatively, this relationship may be an artifact of measurement errors, since undercatch during periods of ridge-top snow and valley rain (as discussed in section 2.2) may distort the observed pattern and lead to the false appearance of reduced enhancement during cold periods.

Figure 16 is equivalent to Figure 15, but was constructed using the archived MM5 output from October 2005 to December 2007. Using the model output avoids the observational uncertainties associated with undercatch of snow, and offers a more continuous dataset resulting in a larger sample size. As for the observations, the pattern shows a temperature dependence, albeit less pronounced. While all temperature bins exhibit the same fundamental pattern of enhanced precipitation on the ridge-top relative to the valleys, this enhancement becomes more subdued with decreasing temperature. Although there is a modest suggestion of increase in lee-side precipitation at low temperature, there is not evidence of a distinct lee-side peak in enhancement, as shown in Figure 12 and Zängl (2007). This may be absent because it is not a dominant and persistent feature of the climatology. Alternatively, it may be an important feature that requires a finer grid spacing than 4 km to be properly resolved.
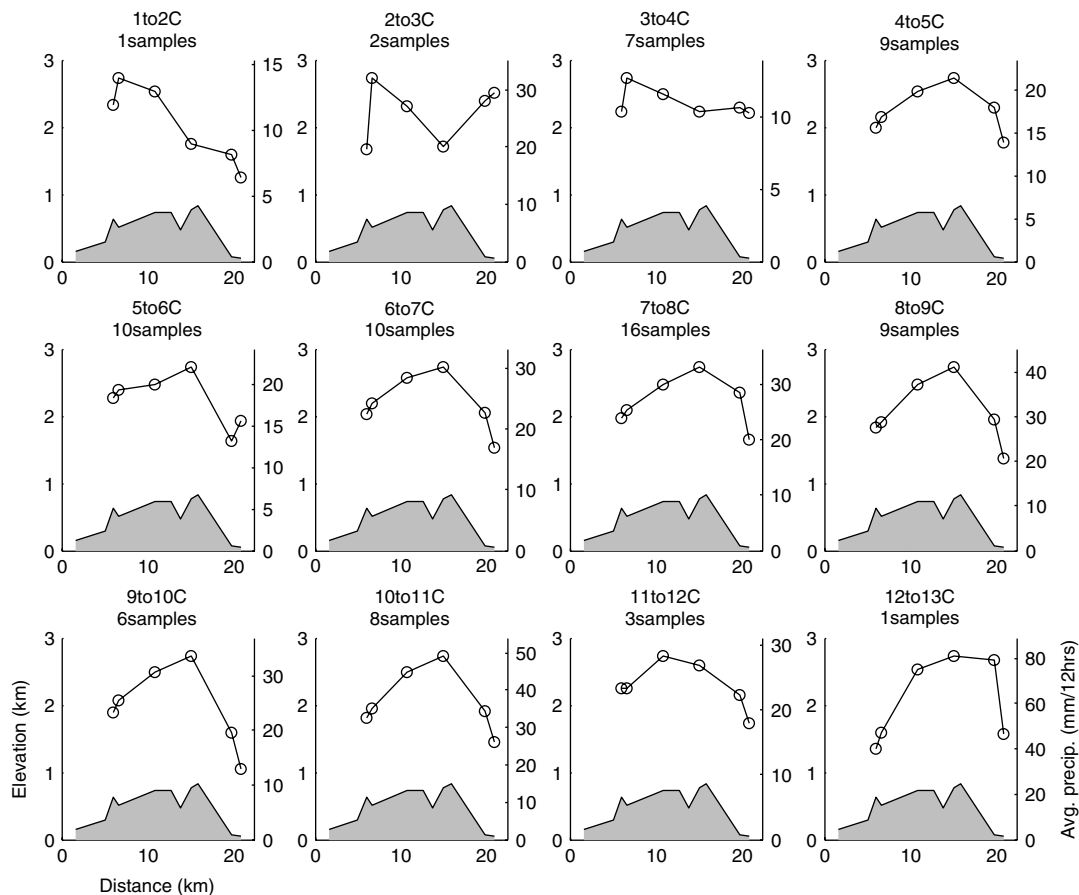

Figure 15. Observed average 12-hour precipitation patterns composited based upon 2 m temperature at BKBW station for the water year 2006 field season. Each figure shows the average 12-hour accumulated precipitation at the gauge sites during periods when the lowland temperatures are within the labelled intervals. The number of events used for each composite is noted as 'samples'. Rainfall events with gauge-network-averaged precipitation rates of less than 6 mm/12 hrs were excluded from the analysis.
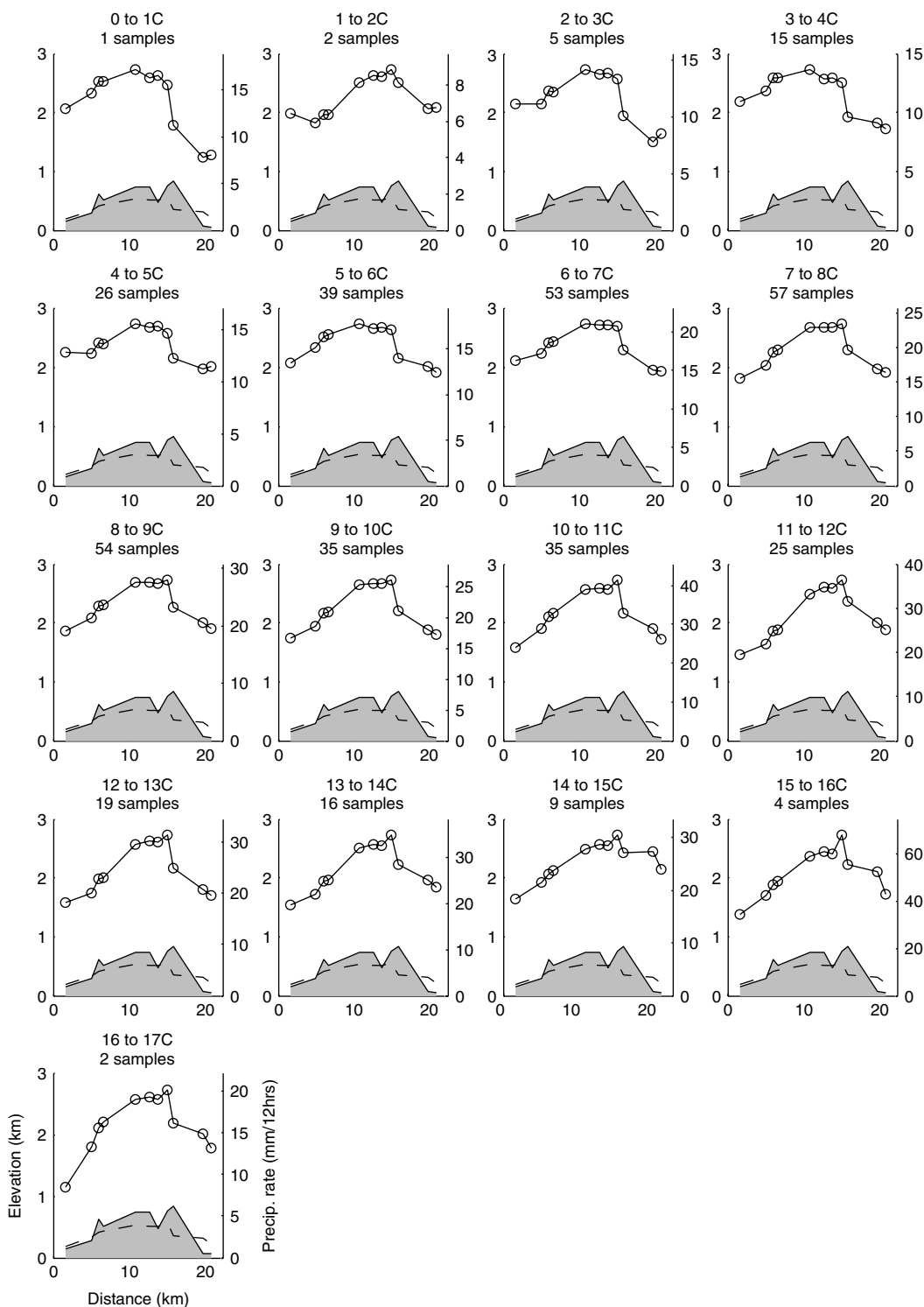
Figure 16. MM5 average 12-hour precipitation patterns composited based upon 2 m temperature simulated at site of BKBW station for Oct 2005 to Dec 2007. Methods and conventions used are equivalent to those for Figure 15.

We have conducted the same compositing using other upwind metrics that would be expected to have bearing upon the pattern of orographic precipitation including 10 m wind speed and wind direction, precipitation rate, and low-level water vapour flux at BKBW. Results (not shown) indicate that, both in MM5 and observations, the basic form and amplitude of the ridge–valley precipitation pattern are remarkably insensitive to changes in the considered parameters. The ridge-top maxima is a pronounced feature both during events with ridge-parallel and ridge-perpendicular winds, for events with a range of wind speeds, and during events with both light and heavy upstream rainfall rates. While there are significant variations in the precipitation pattern, they do not appear to be systematically related to these other parameters in a simple way.

5. Discussion

The consistent pattern of ridge-top enhancement, results from our case study analysis, and aircraft observations during the IMPROVE II field campaign (Garvert *et al.*, 2007) all point to the collection of cloud droplets in low-level wave clouds forced by ascent over individual ridges as the dominant control on precipitation patterns over the western Olympics. Bergeron's conceptual model of the seeder–feeder mechanism aids in explaining the enhancement occurring over the ridges of the Olympics. However, in our simulations, as found in previous work (e.g. Browning *et al.*, 1974), there is no clear separation between synoptically forced clouds and orographically forced clouds, both of which seed and feed the collection process. We also find that the sloping trajectories of hydrometeors play an important role and, during periods of low freezing level, the low fall speeds of frozen hydrometeors can drastically alter the pattern. The cross-ridge flow, which is a major feature of the climatology in the southwestern Olympics (Figure 3), plays a key role in determing the regions of enhancement, and may be related to the blocking of the low-level air on the scale of the entire range. Variations in microphysical parametrizations do not fundamentally alter the ridge–valley enhancement pattern, suggesting it does not depend on complex microphysical interactions for its existence.

Previous studies have identified other physical mechanisms as potentially important components of orographic enhancement, including small-scale turbulence (e.g. Houze and Medina, 2005), banded convection (e.g. Kirshbaum *et al.*, 2007), and lee-side stratification (e.g. Zängl, 2005). While these may be key components of some individual storms, we find that over the western Olympic Mountains they do not need to be invoked in order to understand the basic climatological precipitation pattern on the ridge–valley scale.

In model simulations, the enhancement occurs at very low levels (< 1 km) over the terrain. This suggests that it would be difficult to fully characterize the rainfall using traditional ground-based scanning radar, which must scan at significantly high elevation angles to avoid terrain blockage and ground clutter. Therefore, unless optimally placed, ground-based radar may tend to greatly underestimate surface rainfall over the Olympics (e.g. Kitchen and Blackall, 1992).

The structure of small-scale mountain waves may represent a fundamental control on both precipitation patterns and the efficiency of orographic precipitation. Smith and Barstad (2004) have already examined how linear mountain wave dynamics control orographic precipitation for the case of uniform, stable upstream flow, and their model can be tuned to reproduce well the patterns of precipitation observed over the western Olympics (Anders *et al.*, 2007). However, Smith's model does not represent the inherent nonlinearity associated with the collection processes which constitute the principal source for precipitation over the ridges of the Olympics. Thus, while the linear model provides a simple and elegant representation of the precipitation processes, care must be taken in the physical interpretion of its results since the neglect of nonlinear cloud processes can mask important threshold behaviours (Jiang and Smith, 2003). Directional shear and changes in stability with height may limit the vertical extent of mountain waves and associated orographic clouds. We do not expect the vertical extent of the small-scale wave clouds to have a major bearing upon the small-scale patterns of surface rainfall, since these patterns must be most strongly controlled by the cloud structure in the lowest kilometre or so (since, due to downwind advection, rainfall originating from higher levels cannot consistently translate into patterns as tightly tied to narrow terrain features as we have observed; Bergeron, 1968). However, the depth of the cloud forced by the ridge may affect the amount of enhancement that occurs (e.g. Carruthers and Choularton 1983; Choularton and Perry, 1986) and present a strong control on the efficiency with which moisture is extracted from the incident flow and converted to precipitation (as represented by the 'drying-ratio' metric; Smith *et al.*, 2003).

The robustness of the patterns we have observed in the Olympics lead us to believe that they can likely be generalized to other mountain regions with significant ridge–valley relief that receive much of their precipitation as rain under stable conditions during the passage of midlatitude cyclones. Despite the presence of similar simulated patterns over the Cascades (Figure 2), we have less confidence in generalizing the observed patterns to colder regions. During heavy rainfall in the Olympics, the freezing level is often situated above the height of the windward ridges, and accordingly, the low-level collection responsible for the ridge–valley pattern is not strongly controlled by ice-phase processes. Relative to the Olympics, large biases have been identified in MM5 forecasts over the higher Cascades, perhaps due to the increased importance of ice-phase microphysics. Also, the downwind drift of snow (see Figures 12 and Zängl, 2007) may drastically alter the pattern during cold events. In regions where rainfall from convective events plays a major role, we expect that small-scale patterns may differ notably, as the lack of steady wave clouds, and the presence of features such as banded convection (e.g. Kirshbaum *et al.*, 2007), and transient cells (as discussed in section 3.3) can lead to fundamentally different patterns.

The persistence of the small-scale precipitation patterns in the Olympics provides potential for strong interactions between surface processes and mountain climates. For instance, Anders *et al.* (2008) have coupled a model of surface erosion and a linear model of orographic precipitation (Smith and Barstad, 2004) to show how small-scale patterns of rainfall and topography can co-evolve on geological time-scales. Stolar *et al.* (2007) have examined how the spatial pattern of Olympic mountain precipitation influences uplift, erosion rates, and the shape of the range. Moreover, small-scale patterns of mountain rainfall may act as a control on the pattern of shallow landslide hazard in the Olympic Mountains,

since soil saturation due to extended and/or heavy rainfall is a prime trigger for such landslides (e.g. Caine, 1980).

Key questions remain regarding the importance of various factors in limiting the predictability of mountain precipitation. Deficiencies in model parametrizations (particularly microphysics), horizontal resolution, and initialization have all been cited as major contributors. The excellent agreement between the modelled and observed climatology implies it is unlikely that there are major systematic biases in the model's representation of the fundamental precipitation processes over the region. Yet major shortcomings are present in the model's representation of individual events. For major Olympic mountain storms, the relatively small differences in simulated precipitation between microphysical parametrizations of various complexity suggest that microphysics alone are not the largest source of forecast error in this region. We posit that initial condition errors may impose an important limit on precipitation predictability for many storms. To test this hypothesis requires further work using tools such as ensemble methods to quantify mesoscale predictability limitations arising from uncertainties in upstream initial conditions (e.g. Torn and Hakim, 2007).

6. Summary and conclusions

Analysis of case-studies and climatologies from both dense gauge observations and high-resolution mesoscale model output over the western Olympic Mountains has revealed the following:

- Persistent small-scale patterns of precipitation occur over the ∼10 km wide, ∼800 m high ridges and valleys of the western Olympic Mountains. These patterns are characterized by a 50–60% excess accumulation over the ridges relative to the adjacent valleys in the annual mean.
- The MM5 shows excellent skill in simulating these patterns at seasonal time-scales, however major errors exist for individual storms. These errors are not obviously related to deficiencies in model resolution or microphysics alone, and may be due in part to initial condition errors.
- The mechanism responsible for the ridge-top enhancement of precipitation is similar to Bergeron's conceptual seeder–feeder model. Regions of enhanced condensation of cloud water are produced by ascent in stable flow over the windward slopes of major ridges. Within these clouds, precipitation generated on the synoptic and mesoscale grows by collection, leading to enhanced precipitation which is advected by the prevailing winds.
- Under atypical conditions, fundamental changes in small-scale patterns may occur. During periods of low freezing level, advection of falling snow over the major ridges may lead to a lee-side or valley maximum of precipitation. During unstable conditions the tracks of individual convective cells can play a major role in determining the rainfall pattern.

- Case-studies and composite analysis suggest that departures from the pattern of ridge-top enhancement are rare; the basic patterns and processes appear robust to changes in temperature, winds, and background rainfall rates.

Appendix

Model set-up

For each case-study, hindcasts were completed with MM5 version 3.7.2 in non-hydrostatic mode. Four one-way nested domains were included in the simulation, with horizontal resolutions of 36, 12, 4, and 1.33 km (Figure 6). 33 unevenly-spaced, terrain-following, full sigma levels were used, with increased horizontal resolution in the boundary layer, and a top level located at 100 hPa. A radiative upper-boundary condition (Klemp and Durran, 1983) was applied to prevent unrealistic reflections of gravity waves off the model top. The atmospheric initial and boundary conditions were supplied by interpolation from the NCEP–NCAR reanalyzes (2.5° × 2.5° horizontal resolution; Kalnay *et al.*, 1996). The model terrain and land-use data were formed by interpolating US Geological Survey data (with 5-minute resolution on the 36 km domain, and 30 sec resolution on the inner domains), via a Cressman-type analysis scheme and a two-pass smoother–desmoother. Initial conditions for snow cover as well as subsurface soil temperature and moisture were provided by analysis grids from NCEP's Eta 221 model (with 40 km horizontal spacing), while sea surface temperatures were provided from the US Navy Optimum Interpolation System (OTIS) (with 0.25° horizontal resolution).

As we are interested in the small-scale precipitation processes during given large-scale conditions, we nudged the outermost domain towards the reanalysis grid to force the large-scale flow to evolve similarly to our best

estimate of what actually occurred. This nudging was accomplished via the Four-Dimensional Data Assimilation scheme, using Newtonian relaxation of temperature, zonal and meridional winds, and moisture towards the values from the reanalysis grids (Stauffer and Seaman, 1990). Within the boundary layer, moisture was not nudged.

The Medium-Range Forecast Planetary Boundary Layer (PBL) scheme was used on all domains to account for turbulent processes in the PBL (Hong and Pan, 1996). Short- and long-wave radiative transfer were parametrized via the CCSM radiation scheme (Hack *et al*., 1993). Consistent with the current set-up of the operational Pacific Northwest MM5, Kain–Fritsch convective parametrization was used on all but the innermost (1.33 km) domain, to parametrize unresolved convective motions and associated precipitation (Kain, 2004). Parametrized convective precipitation was minimal during the events simulated. Our principal case-study was run with and without convective parameterization on the 4 km domain, which only resulted in very minimal changes in storm total precipitation.

All runs were completed with three different microphysical schemes. The schemes vary widely in complexity and number of physical processes included, thus we use them to determine relevant processes controlling the observed pattern, and to roughly assess the sensitivity of the simulated precipitation distribution to the microphysical parametrization used. The Reisner2 scheme v3.7 (Reisner *et al*., 1998; Thompson *et al*., 2004) was used as our best representation of the microphysical processes taking place in the atmosphere. It is a bulk microphysical scheme which predicts mixing ratios of water vapour, cloud liquid water, cloud ice, snow, rain, and graupel, as well as the number concentration of cloud ice. The Simple Ice scheme (Dudhia, 1989) predicts the same mixing ratios as Reisner2, except for graupel, which is omitted. Liquid and frozen water do not coexist in this scheme, and there are many fewer interactions between different species of condensed and frozen water. It was used in part to determine the importance of the complex interactions between frozen and liquid water species included in Reisner2 for determining the precipitation pattern. The Warm Rain scheme has a formulation that is very similar to Simple Ice, except all water is assumed to be in the liquid (or vapour) phase. It is quite physically unrealistic for the events we consider, since frozen precipitation processes are certainly occurring, but was used to test the range of responses in the small-scale precipitation pattern to changes in microphysical parametrization.

For comparison to gauge and station data, the MM5 forecasts were interpolated to point locations using bilinear interpolation.

References

Alpert P, Shafir H, Cotton W. 1994. Prediction of meso-γ scale orographic precipitation. *Trends Hydrol.* **1**: 403–441.

Anders AM, Roe GH, Hallet B, Montgomery DR, Finnegan N, Putkonen J. 2006. Spatial patterns of precipitation and topography in the Himalaya. Pp 39–53 in *Tectonics, Climate, and Landscape Evolution*, Willett S, Hovius N, Brandon M, Fisher D. (eds.) Special paper 398, Geological Society of America: Boulder, USA.

Anders AM, Roe GH, Durran DR, Minder JM. 2007. Small-scale spatial gradients in climatological precipitation on the olympic peninsula. *J. Hydrometeorol.* **8**: 1068–1081.

Anders AM, Roe GH, Montgomery DR, Hallet B. 2008. Coupled evolution of topography and orographic precipitation in varied climates. *Geology* in press.

Bergeron T. 1968. On the low-level distribution of atmospheric water caused by orography. *Int. Cloud Phys. Conf.*, Toronto, 96–100.

Bougeault P, Binder P, Buzzi A, Dirks R, Houze R, Kuettner J, Smith RB, Steinacker R, Volkert H. 2001. The MAP special observing period. *Bull. Am. Meteorol. Soc.* **82**: 433–462.

Browning KA, Hill FF, Pardoe CW. 1974. Structure and mechanism of precipitation and effect of orography in a wintertime warm sector. *Q. J. R. Meteorol. Soc.* **100**: 309–330.

Bruintjes RT, Clark TL, Hall WD. 1994. Interactions between topographic air-flow and cloud/precipitation development during the passage of a winter storm in Arizona. *J. Atmos. Sci.* **51**: 48–67.

Caine N. 1980. The rainfall intensity-duration control of shallow landslides and debris flows. *Geografiska Annaler Series A – Phys. Geog.* **62**: 23–27.

Carruthers DJ, Choularton TW. 1983. A model of the feeder–seeder mechanism of orographic rain including stratification and wind-drift effects. *Q. J. R. Meteorol. Soc.* **109**: 575–588.

Choularton TW, Perry SJ. 1986. A model of the orographic enhancement of snowfall by the seeder–feeder mechanism. *Q. J. R. Meteorol. Soc.* **112**: 335–345.

Colle BA. 2008. Two-dimensioal idealized simulations of the impact of multiple windward ridges on orographic precipitation. *J. Atmos. Sci.* **65**: 509–523.

Colle BA, Mass CF. 1996. An observational and modeling study of the interaction of low-level southwesterly flow with the Olympic mountains during COAST IOP 4. *Mon. Weather Rev.* **124**: 2152–2175.

Colle BA, Yuter SE. 2007. The impact of coastal boundaries and small hills on the precipitation distribution across southern Connecticut and Long Island, New York. *Mon. Weather Rev.* **135**: 933–954.

Colle BA, Mass CF, Westrick KJ. 2000. MM5 precipitation verification over the pacific northwest during the 1997–99 cool seasons. *Weather and Forecasting* **15**: 730–744.

Colle BA, Garvert MF, Wolfe JB, Mass CF, Woods CP. 2005. The 13–14 December 2001 IMPROVE-2 event. Part III: Simulated microphysical budgets and sensitivity studies. *J. Atmos. Sci.* **62**: 3535–3558.

Conway H, Raymond CF. 1993. Snow stability during rain. *J. Glaciol.* **39**: 635–642.

Doyle JD, Jiang QF. 2006. Observations and numerical simulations of mountain waves in the presence of directional wind shear. *Q. J. R. Meteorol. Soc.* **132**: 1877–1905.

Dudhia J. 1989. Numerical study of convection observed during the winter monsoon experiment using a mesoscale two-dimensional model. *J. Atmos. Sci.* **46**: 3077–3107.

Durran DR, Klemp JB. 1982. On the effects of moisture on the Brunt–Väisälä frequency. *J. Atmos. Sci.* **39**: 2152–2158.

Frei C, Schär C. 1998. A precipitation climatology of the Alps from high-resolution rain-gauge observations. *Int. J. Climatol.* **18**: 873–900.

Fuhrer O, Schär C. 2005. Embedded cellular convection in moist flow past topography. *J. Atmos. Sci.* **62**: 2810–2828.

Garvert MF, Smull BF, Mass CF. 2007. Multiscale mountain waves influencing a major orographic precipitation event. *J. Atmos. Sci.* **64**: 711–737.

Grell G, Dudhia J, Stauffer DR. 1995. Description of the fifth-generation Penn State/NCAR mesoscale model (MM5). Tech. Note NCAR/TN-398+STR. NCAR: Boulder, USA. http://www.mmm.ucar.edu/mm5/documents/mm5-desc-doc.html.

Groisman PY, Legates DR. 1994. The accuracy of United States precipitation data. *Bull. Am. Meteorol. Soc.* **75**: 215–227.

Grubišić V, Vellore RK, Huggins AW. 2005. Quantitative precipitation forecasting of wintertime storms in the Sierra Nevada: Sensitivity to the microphysical parameterization and horizontal resolution. *Mon. Weather Rev.* **133**: 2834–2859.

Hack JJ, Boville BA, Briegleb BP, Kiehl JT, Rasch PJ, Williamson DL. 1993. Description of the NCAR Community Climate Model (CCM2). Technical Note NCAR/TN-382+STR. NCAR: Boulder, USA.

Hill FF, Browning KA, Bader MJ. 1981. Radar and rain-gauge observations of orographic rain over South Wales. *Q. J. R. Meteorol. Soc.* **107**: 643–670.

Hobbs PV. 1975. The nature of winter clouds and precipitation in the Cascade Mountains and their modification by artificial seeding. 1. Natural conditions. *J. Appl. Meteorol.* **14**: 783–804.

Hobbs PV, Easter RC, Fraser AB. 1973. Theoretical study of flow of air and fallout of solid precipitation over mountainous terrain: Part II Microphysics. *J. Atmos. Sci.* **30**: 813–823.

Hong SY, Pan HL. 1996. Nonlocal boundary layer vertical diffusion in a medium-range forecast model. *Mon. Weather Rev.* **124**: 2322–2339.

Houze RA, Medina S. 2005. Turbulence as a mechanism for orographic precipitation enhancement. *J. Atmos. Sci.* **62**: 3599–3623.

Houze RA, James CN, Medina S. 2001. Radar observations of precipitation and airflow on the mediterranean side of the alps: Autumn 1998 and 1999. *Q. J. R. Meteorol. Soc.* **127**: 2537–2558.

Jiang QF. 2003. Moist dynamics and orographic precipitation. *Tellus A* **55**: 301–316.

Jiang QF, Smith RB. 2003. Cloud timescales and orographic precipitation. *J. Atmos. Sci.* **60**: 1543–1559.

Kain JS. 2004. The Kain–Fritsch convective parameterization: An update. *J. Appl. Meteorol.* **43**: 170–181.

Kalnay E, Kanamitsu M, Kirtler R, Collins W, Deaven D, Gandin L, Iredell M, Saha S, White G, Woollen J, Zhu Y, Chelliah M, Ebisuzaki W, Higgins W, Janowiak J, Mo KC, Ropelewski C, Wang J, Leetma A, Reynolds R, Jenne R, Joseph D. 1996. The NCEP/NCAR 40-year reanalysis project. *Bull. Am. Meteorol. Soc.* **77**: 437–471.

Kirshbaum DJ, Durran DR. 2004. Factors governing cellular convection in orographic precipitation. *J. Atmos. Sci.* **61**: 682–698.

Kirshbaum DJ, Bryan G, Rottuno R, Durran DR. 2007. The triggering of orographic rainbands by small-scale topography. *J. Atmos. Sci.* **64**: 1530–1549.

Kitchen M, Blackall RM. 1992. Orographic rainfall over low hills and associated corrections to radar measurements. *J. Hydrol.* **139**: 115–134.

Klemp JB, Durran DR. 1983. An upper boundary-condition permitting internal gravity-wave radiation in numerical mesoscale models. *Mon. Weather Rev.* **111**: 430–444.

Marwitz JD. 1987. Deep orographic storms over the Sierra Nevada: 2. The precipitation processes. *J. Atmos. Sci.* **44**: 174–185.

Mass CF, Albright M, Ovens D, Steed R, MacIver M, Grimit E, Eckel T, Lamb B, Vaughan J, Westrick K, Storck P, Colman B, Hill C, Maykut N, Gilroy M, Ferguson SA, Yetter J, Sierchio JM, Bowman C, Stender R, Wilson R, Brown W. 2003. Regional environmental prediction over the Pacific Northwest. *Bull. Am. Meteorol. Soc.* **84**: 1353–1366.

McCaughey WW, Farnes PE. 1996. 'Measuring winter precipitation with an antifreeze-based tipping-bucket gauge'. Pp 130–136 in Proceedings of 64th Western Snow Conference, Bend, Oregon.

Medina S, Houze RA. 2003. Air motions and precipitation growth in Alpine storms. *Q. J. R. Meteorol. Soc.* **129**: 345–371.

Mote PW, Hamlet AF, Clark MP, Lettenmaier DP. 2005. Declining mountain snowpack in western North America. *Bull. Am. Meteorol. Soc.* **86**: 39–49.

Pierrehumbert RT, Wyman B. 1985. Upstream effects of mesoscale mountains. *J. Atmos. Sci.* **42**: 977–1003.

Reisner J, Rasmussen RM, Bruintjes RT. 1998. Explicit forecasting of supercooled liquid water in winter storms using the MM5 mesoscale model. *Q. J. R. Meteorol. Soc.* **124**: 1071–1107.

Roe GH, Montgomery DR, Hallet B. 2002. Effects of orographic precipitation variations on the concavity of steady-state river profiles. *Geology* **30**: 143–146.

Rotunno R, Houze RA. 2007. Lessons on orographic precipitation for the Mesoscale Alpine Programme. *Q. J. R. Meteorol. Soc.* **133**: 811–830.

Shutts GJ. 1998. Stationary gravity-wave structure in flows with directional wind shear. *Q. J. R. Meteorol. Soc.* **124**: 1421–1442.

Sinclair MR, Wratt DS, Henderson RD, Gray WR. 1997. Factors affecting the distribution and spillover of precipitation in the southern Alps of New Zealand – A case study. *J. Appl. Meteorol.* **36**: 428–442.

Smith RB. 1979. The influence of mountains on the atmosphere. *Adv. Geophys.* **21**: 87–230.

Smith RB, Barstad I. 2004. A linear theory of orographic precipitation. *J. Atmos. Sci.* **61**: 1377–1391.

Smith RB, Jiang QF, Fearon MG, Tabary P, Dorninger M, Doyle JD, Benoit R. 2003. Orographic precipitation and air mass transformation: An Alpine example. *Q. J. R. Meteorol. Soc.* **129**: 433–454.

Stauffer DR, Seaman NL. 1990. Use of 4-dimensional data assimilation in a limited-area mesoscale model: Part I. Eexperiments with synoptic-scale data. *Mon. Weather Rev.* **118**: 1250–1277.

Stoelinga MT, Hobbs PV, Mass CF, Locatelli JD, Colle BA, Houze RA, Rangno AL, Bond NA, Smull BF, Rasmussen RM, Thompson G, Colman BR. 2003. Improvement of microphysical parameterization through observational verification experiment. *Bull. Am. Meteorol. Soc.* **84**: 1807–1826.

Stolar D, Roe G, Willett S. 2007. Controls on the patterns of topography and erosion rate in a critical orogen. *J. Geophys. Res.* **112**: F04002, DOI: 10.1029/2006JF000713.

Thompson G, Rasmussen RM, Manning K. 2004. Explicit forecasts of winter precipitation using an improved bulk microphysics scheme. Part I: Description and sensitivity analysis. *Mon. Weather Rev.* **132**: 519–542.

Torn RD, Hakim GJ. 2007. Ensemble-based sensitivity analysis. *Mon. Weather Rev.* **136**: 663–677.

Tustison B, Harris D, Foufoula-Georgiou E. 2001. Scale issues in verification of precipitation forecasts. *J. Geophys. Res.–Atmos.* **106**: 11775–11784.

Walser A, Schär C. 2004. Convection-resolving precipitation forecasting and its predictability in Alpine river catchments. *J. Hydrol.* **288**: 57–73.

Wang JH, Cole HL, Carlson DJ, Miller ER, Beierle K, Paukkunen A, Laine TK. 2002. Corrections of humidity measurement errors from the Vaisala RS80 radiosonde – application to TOGA COARE data. *J. Atmos. Oceanic Technol.* **19**: 981–1002.

Westrick KJ, Mass CF. 2001. An evaluation of a high-resolution hydrometeorological modeling system for prediction of a cool-season flood event in a coastal mountainous watershed. *J. Hydrometeorol.* **2**: 161–180.

Willett SD. 1999. Orogeny and orography: The effects of erosion on the structure of mountain belts. *J. Geophys. Res.–Solid Earth* **104**: 28957–28981.

Yang DQ, Goodison BE, Metcalfe JR, Golubev VS, Bates R, Pangburn T, Hanson CL. 1998. Accuracy of NWS 8 inch standard non-recording precipitation gauge: Results and application of WMO intercomparison. *J. Atmos. Oceanic Technol.* **15**: 54–68.

Zängl G. 2005. The impact of lee-side stratification on the spatial distribution of orographic precipitation. *Q. J. R. Meteorol. Soc.* **131**: 1075–1091.

Zängl G. 2007. Interaction between dynamics and cloud microphysics in orographic precipitation enhancement: A high-resolution modeling study of two north Alpine heavy-precipitation events. *Mon. Weather Rev.* **135**: 2817–2840.